






Measurement of the $^{239}\text{Pu}(n, f)$ prompt fission neutron spectrum from 10 keV to 10 MeV induced by neutrons of energy 1–20 MeV

K. J. Kelly ^{1,*}, M. Devlin,¹ J. M. O'Donnell,¹ J. A. Gomez,¹ D. Neudecker,¹ R. C. Haight,¹ T. N. Taddeucci,¹ S. M. Mosby,¹ H. Y. Lee,¹ C. Y. Wu,² R. Henderson,² P. Talou ¹, T. Kawano,¹ A. E. Lovell ¹, M. C. White,¹ J. L. Ullmann ¹, N. Fotiades ¹, J. Henderson,² and M. Q. Buckner²

¹Los Alamos National Laboratory, Los Alamos, New Mexico 87545, USA

²Lawrence Livermore National Laboratory, Livermore, California 94550, USA



(Received 9 March 2020; accepted 29 July 2020; published 21 September 2020)

Although the prompt fission neutron spectrum (PFNS) is an essential component of neutron-driven systems that has been measured for decades, there are still multiple glaring unknowns regarding the PFNS of major actinides in the fission neutron incident energy range, specifically with regard to multichance fission and pre-equilibrium neutron emission processes. The only impactful experimental ^{239}Pu PFNS measurements included in recent nuclear data evaluations were measured over a limited outgoing neutron energy range at thermal and 1.5-MeV average incident neutron energy, while other potentially impactful measurements have been shown to contain errors that resulted in either large uncertainty increases or in complete exclusion from nuclear data evaluation. We report here a measurement of the ^{239}Pu PFNS over a wide range of incident neutron energy (1–20 MeV) and three orders of magnitude in outgoing neutron energy (0.01–10 MeV) resulting from the Chi-Nu experiment at the Los Alamos Neutron Science Center. These results are the combination of separate PFNS measurements in the same experimental area, one using a Li-glass and the other a liquid scintillator detector array. Covariances between all PFNS data points from each detector and within each incident energy range were generated between all other data in *both* detector arrays and within *all* other incident neutron energy bins, yielding a single covariance matrix for all 1300 PFNS data points reported here. These covariances are based on a thorough assessment of systematic bias and uncertainties associated with the measurement, PFNS extraction technique, combination of data from each detector type, and other aspects of the analysis. The existence of covariances between PFNS data points in different incident neutron energy ranges yielded covariances between average PFNS energy values at each incident energy to be reported here as well, which allowed for firm statements to be made regarding a *shape* of a purely experimental mean PFNS energy trend for the first time. Although minor PFNS shape differences exist between the results reported here and recent nuclear data evaluations, the ENDF/B-VIII.0 and JEFF-3.3 PFNS evaluations agree reasonably well with the present results from 1- to 10-MeV incident neutron energy, which spans the well-measured 1.5-MeV incident neutron energy PFNS from Lestone and Shores as well as the onset of second-chance fission. However, while the pre-equilibrium component of the PFNS above 12-MeV incident neutron energy roughly agrees in position and magnitude with ENDF/B-VIII.0 and JEFF-3.3, clear differences relating to the relative magnitude of third-chance fission PFNS features are present in the PFNS shape and in the mean PFNS energy trends.

DOI: [10.1103/PhysRevC.102.034615](https://doi.org/10.1103/PhysRevC.102.034615)

I. INTRODUCTION

The complexity of nuclear fission requires fission models to rely heavily on experimental measurements of fission observables. In terms of fission-driven chain reactions, the energy spectrum of prompt neutrons from neutron-induced fission, known as the prompt fission neutron spectrum (PFNS), is of clear importance. It is especially of interest also for innovative nuclear fuels in breeder reactors and fast reactors in general [1]. While it is the spectrum of neutrons emitted promptly following fission that is commonly described when discussing the PFNS, the experimentally observed spectra

contain neutrons that were emitted both before (prefission) and after (postfission) the fission event. There may also be “scission neutrons” emitted during the fission process. PFNS models have been developed for decades and range from simple neutron evaporation models, such as Maxwellian and Watt distributions [2,3], to more complicated descriptions like the Los Alamos Model (LAM) [4], those contained in the CGMF [5] and FREYA [6] codes, analog Hauser-Feshbach calculations [7–9], statistical approaches [10], and others. It is unclear whether any of these approaches accurately describe the ^{239}Pu PFNS on the basis of the available data.

Capote *et al.* [11] and Neudecker *et al.* [12,13] provided a thorough description of the available experimental ^{239}Pu PFNS data as well as those data suitable for incorporation into the ENDF/B evaluations [14,15], and so only the

*Corresponding author: kkelly@lanl.gov

relevant details will be discussed here. Note that here and throughout this work, E_n^{out} refers to the measured outgoing neutron energy from fission and E_n^{inc} refers to the incident neutron beam energy that induced the fission event. Lestone and Shores [16] determined the PFNS for a series of discrete outgoing energies ranging from $E_n^{\text{out}} = 1.5\text{--}10.5$ MeV for an average incident neutron energy of $\langle E_n^{\text{inc}} \rangle = 1.5$ MeV, and these data heavily influence the ENDF/B evaluations at these energies [14,15]. Staples [17] measured the ^{239}Pu PFNS for the incident and outgoing neutron energy ranges $E_n^{\text{inc}} = 0.5$ MeV and $E_n^{\text{out}} = 0.596\text{--}15.952$ MeV, $E_n^{\text{inc}} = 1.5$ MeV and $E_n^{\text{out}} = 1.696\text{--}15.192$ MeV, $E_n^{\text{inc}} = 2.5$ MeV and $E_n^{\text{out}} = 2.808\text{--}14.485$ MeV, and $E_n^{\text{inc}} = 3.5$ MeV and $E_n^{\text{out}} = 4.088\text{--}13.828$ MeV. While these data initially appear to make a significant contribution to the database of ^{239}Pu PFNS data, it was determined that there may have been an issue with the employed detector efficiency, and corrections for multiple scattering were also missing. So these data were later reanalyzed by Lestone [18] and scaled according to the efficiency curve used for the ^{235}U PFNS measurements by Johansson and Holmqvist [19]. The uncertainties associated with this correction were determined to be substantial enough for these data to be excluded from the ENDF/B-VIII.0 evaluation [13,15]. Chatillon *et al.* [20] reported the ^{239}Pu PFNS from $E_n^{\text{inc}} = 1\text{--}200$ MeV and $E_n^{\text{out}} = 0.4\text{--}7$ MeV, but their data were also called into question with regard to their assumed efficiency curve. As a result, the data from Chatillon *et al.* were corrected by Granier [21] and additional systematic uncertainties were included on these data when used in the ENDF/B-VIII.0 evaluation [13,15]. However, due to the fact that Chatillon *et al.* did not observe the pre-equilibrium peak of their PFNS spectrum, their measurement above $E_n^{\text{inc}} = 15$ MeV was excluded from ENDF/B-VIII.0 altogether.

Realistic estimates of the precision from a decadal experiment need to be considered prior to the measurement campaign to ensure that the results will have a significant impact on nuclear data evaluations. These uncertainty estimates were set as goals nearly 10 years prior to this work during the development of the Chi-Nu project and were chosen to be 5%, 3%, 5%, and 15% for measurements of PFNS neutrons at $E_n^{\text{out}} = 0.1\text{--}1.0$, $1.0\text{--}5.0$, $5.0\text{--}8.0$, and $8.0\text{--}10.0$ MeV, respectively [22–24]. While ambitious, these goals were noticeably larger than the total uncertainty of the latest ENDF/B evaluation at the time, ENDF/B-VII.0 [25]. With the development of ENDF/B-VII.1 [14] and ENDF/B-VIII.0 [15], these evaluated uncertainties have since been increased [26] to be typically in the range of 5–10%, 1.5–2%, and 15–30% at $E_n^{\text{out}} = 0.1$, 2.0, and 10 MeV, respectively, for the ENDF/B-VIII.0 ^{239}Pu PFNS evaluation. Thus, the target uncertainty goals for results from the Chi-Nu project align well with the uncertainties in the latest evaluations, and are therefore poised to make a significant contribution to the evaluated database, especially given that measurements for incident neutron energy ranges in which there are either very few or no measurements are provided.

It is important to note that a report of data from Marini *et al.* was recently published in Ref. [27]. Although the results shown in the present work are intrinsically correlated to those of Ref. [27] because they were collected using the

same liquid scintillator detector array used here and within the same experimental flight path, the fission-counter target, detector shielding, data acquisition, and analysis are unique to each experiment. The results shown here were obtained using data from an experiment that is completely separate from that of Ref. [27] and the analysis of these data sets was carried out independently. While the comparison of these correlated works is of interest to the community, this comparison is beyond the scope of this paper and will be presented in a future paper.

In this work, we present data collected on the ^{239}Pu PFNS for $E_n^{\text{inc}} = 1\text{--}20$ MeV and $E_n^{\text{out}} = 0.01\text{--}10$ MeV at the Weapons Neutron Research (WNR) facility, which is part of the Los Alamos Neutron Science Center (LANSCE) at Los Alamos National Laboratory. Outgoing neutrons with an energy below ≈ 1.5 MeV were measured with a Li-glass detector array while those with an energy above ≈ 0.85 MeV were measured with an array of liquid scintillator detectors. Data from these arrays were collected in separate experiments and combined to form a single measurement of the PFNS shape over the specified outgoing neutron energy range. Details of the experimental setup are given in Sec. II A and those on background treatment are discussed in Sec. II B. With regard to detector characterization, a highly detailed Monte Carlo simulation was created with the general Monte Carlo N-Particle transport code (MCNP®) and modified to match each experimental configuration prior to data analysis. The use of this simulation eliminated the need for determination of a detector efficiency curve. The Chi-Nu MCNP model is described in Sec. II C with assessment of the fission counter efficiency in Sec. II D, a description of the general procedure for extracting the PFNS results in Sec. II E, and corrections for neutron beam wraparound effects in Sec. II F. Data reduction procedures are unique for each detector type used at Chi-Nu. Li-glass and liquid scintillator data analysis procedures are described in Secs. III A and IV A, respectively.

In addition to performing a high-statistics measurement of the PFNS, we strived to provide a thorough statistical and systematic uncertainty analysis completed with covariance matrices for each uncertainty source, as well as for the PFNS shape result from each detector array. These uncertainties are described in Secs. III B and IV B for Li-glass and liquid scintillator data, respectively. However, the PFNS shapes from the Li-glass and liquid scintillator arrays correspond to different portions of the same total PFNS shape and the same underlying PFNS shape is probed in the overlapping outgoing neutron energy region between these two detector arrays. The shapes from these detector arrays are therefore combined to form a single PFNS result across all measured outgoing energy ranges according to the methods described in Ref. [28]. Furthermore, not only are the data correlated across all measured outgoing neutron energies, but they are also correlated across all measured incident energies. This correlation has never been measured or quantified for an experimental PFNS measurement and allows for separate assessments of the Chi-Nu PFNS results in terms of both relative PFNS value *and shape* across incident neutron energies. Both the combination of data from the Li-glass and liquid scintillator arrays and the correlation of the data across all measured incident energy

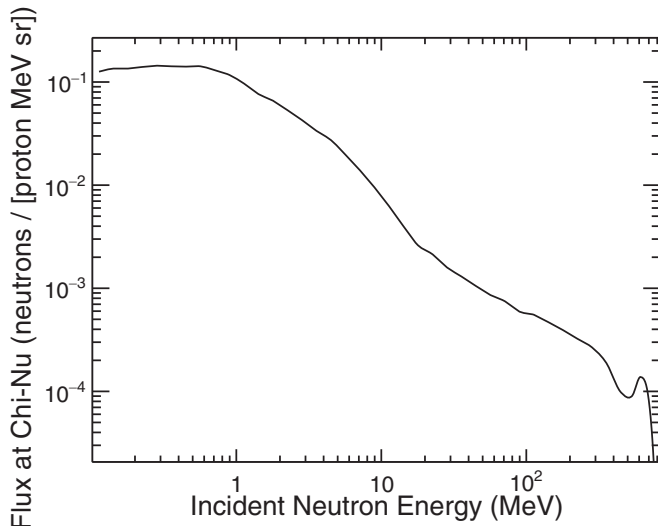


FIG. 1. The neutron flux at the Chi-Nu target position based on an MCNP calculation of neutron emission from the tungsten spallation target following irradiation with the nominal proton beam at WNR is shown here. Note that attenuation along the target flight path reduces the low-energy flux compared to what is shown in this calculation.

ranges are described in Sec. V. Results are shown in Sec. VI in terms of PFNS comparisons with evaluations, with spectra below $E_n^{\text{inc}} = 5$ MeV shown in Sec. VI A, $5 \text{ MeV} \leq E_n^{\text{inc}} \leq 10$ MeV in Sec. VI B, and $10 \text{ MeV} \leq E_n^{\text{inc}} \leq 20$ MeV in Sec. VI C. Finally, the primary conclusions of this work are discussed in Sec. VII.

II. THE Chi-Nu EXPERIMENT

A. Experimental configuration

Additional details of the Chi-Nu experimental area can be found in Ref. [29,30]. Only the necessary details will be repeated here. The incident neutron beam at LANSCE/WNR originates from proton spallation reactions on a tungsten target 21.5 m upstream of the Chi-Nu target position, and 15° to the left of the incident proton beam direction. The signal indicating a proton interaction with the tungsten target, measured at a time referred to as t_0 , is collected and stored for incident neutron energy calculations via time of flight. A calculation of the nominal incident neutron beam production at the Chi-Nu target position is shown in Fig. 1.

Incident neutrons of a 2-cm radius beamspot size reach a parallel-plate avalanche counter (PPAC) [31] chamber containing 10 individual PPAC volumes. Each volume is separated from neighboring volumes by a $5\text{-}\mu\text{m}$ platinum plate and consists of a titanium foil with 5 mg of $>99.9\%$ pure ^{239}Pu electro-deposited on either side. Each deposit is 4 cm in diameter, yielding a target density of approximately $400 \mu\text{g}/\text{cm}^2$ for each volume. Fission fragments from neutron induced fission of ^{239}Pu are then detected via an electron avalanche initiated by ionization of 4.2-torr isobutane gas within the PPAC chamber and generated via a 375-V potential difference between two aluminum foils. A ^{252}Cf PPAC chamber with an

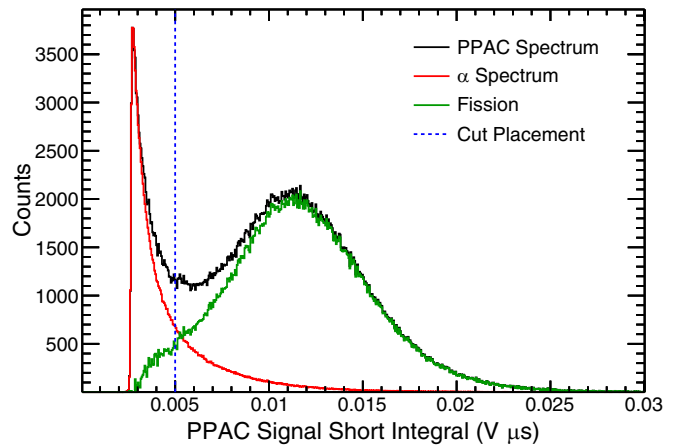


FIG. 2. An example PPAC integral spectrum is shown here. This is the observed spectrum from a single PPAC volume after the analyses described in Secs. III A and IV A.

identical construction and only a single PPAC cell was also fabricated for experimental and simulation calibration tests (see Sec. II C for more details). The difference between the fission fragment detection time, t_f , and the neutron production time, t_0 , yields the incident neutron energy, E_n^{inc} . The fast (<1.0 ns) time resolution of the PPAC signals yields a 0.36% uncertainty on the time-of-flight of a 20 MeV incident neutron, which corresponds to a 0.58% uncertainty on the incident neutron energy. This uncertainty rapidly decreases with decreasing incident neutron energy, and so the uncertainty on the incident neutron beam energy can be ignored for the results shown in this work. In addition to fission fragments, the PPAC detects α particles that are spontaneously emitted from ^{239}Pu at a rate of $\approx 1.1 \times 10^7 \alpha/\text{s}$ per ^{239}Pu deposit [31]. This created a time-independent background that will be addressed in Sec. II B. An example PPAC spectrum for a single PPAC volume during the course of this experiment is shown in Fig. 2. While the α background does contaminate the region containing fission signals of interest, this background is addressed with the method described in Sec. II B, the separation between α particles and fission fragments is clearly seen, and approximately 95% of the fissions detected in coincidence with both a neutron and a t_0 signal were able to be extracted for data analysis.

The results shown in this work were collected over the course of two separate but correlated experiments. Neutrons below $E_n^{\text{out}} = 1.59$ MeV were detected with a 22-detector Li-glass array, shown in Fig. 3. Of the 22 Li-glass detectors, 21 of them are GS20 Li-glass (95% enriched with ^6Li) with the remaining detector made of GS30 Li-glass (99.9% enriched in ^7Li), both of which were purchased from Scintacor [32,33] and each of which was mounted to an R1250A Hamamatsu photomultiplier tube (PMT) [34]. Five of these detectors contain 1.27-cm-thick Li-glass while the others are 1.80 cm thick. The nominal flight path distance from the PPAC to a Li-glass detector is 0.400(5) m with a net $1\text{-}\sigma$ outgoing-neutron time resolution of 1.03(1) ns. The ^{239}Pu Li-glass results presented here were collected over 1650 h, yielding 1322 h of usable data and approximately 1.43×10^{10}

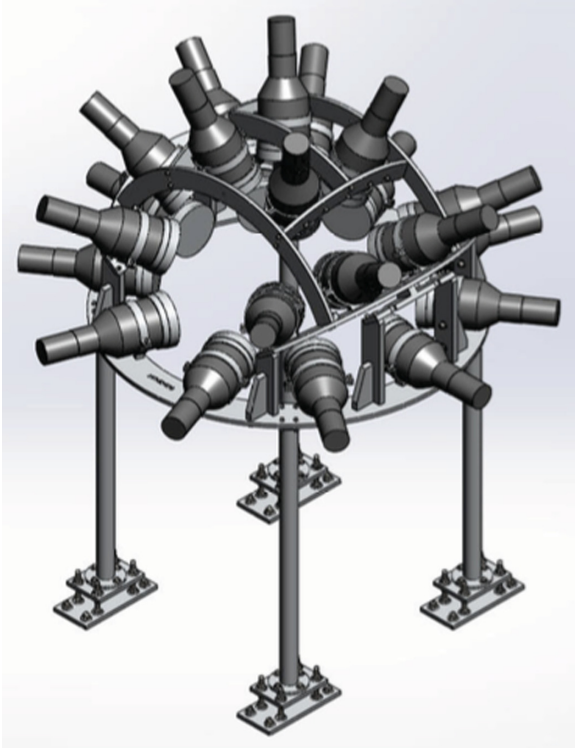


FIG. 3. A rendering of the Chi-Nu Li-glass detector array is shown here. Beam enters from the lower-left of this figure. The PPAC fission counter is at the center of the array.

total fission events. Neutrons above $E_n^{\text{out}} = 0.89$ MeV were collected with a 54-detector EJ-309 [35] liquid scintillator array, shown in Fig. 4, with each detector optically coupled to an R4144 Hamamatsu PMT. Each liquid scintillator is a

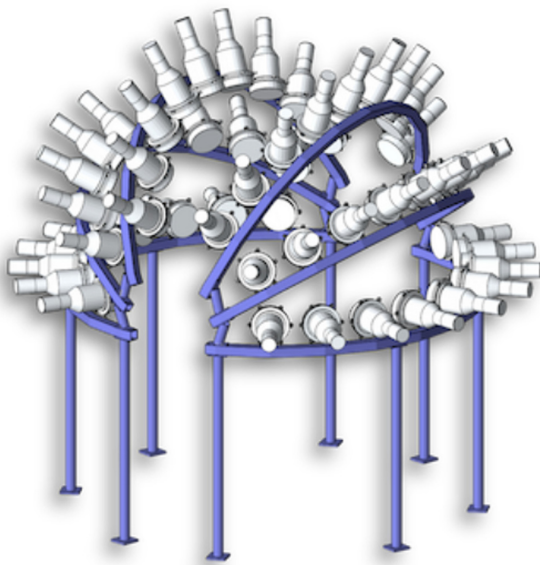


FIG. 4. A rendering of the Chi-Nu liquid scintillator detector array is shown here. Beam enters from the lower-left of this figure. The PPAC fission counter is at the center of the array.

5.5-cm-thick \times 17.7-cm diameter cylindrical volume with a nominal flight path of 1.020(5) m from the PPAC to the detector center and net $1\text{-}\sigma$ outgoing-neutron time resolution of 1.05(1) ns. The ^{239}Pu liquid scintillator data presented in this work were collected over 518 h, yielding 412 h of usable data and approximately 1.28×10^9 total fission events. It is primarily the differences in beam intensity between the two experiments that impacts the relative number of fission events. Details of Li-glass and liquid scintillator detector spectra and analysis are discussed in Secs. III A and IV A, respectively. High voltages for detector PMTs were supplied via a CAEN SY4527 HV supply [36]. Signals from all neutron detectors, each PPAC volume, and the t_0 timing were asynchronously read out with a series of CAEN 1730b digitizers [37] using MIDAS [38]. Time stamps and integral information for each pulse were available at all stages of offline analysis. Dead time was negligible for this experiment given the relatively fast pulses from these detector arrays and the asynchronous digital data acquisition system employed here. Neutron signals detected at a time, t_n , were used to assign outgoing neutron energies from time of flight using the $t_n - t_f$ time difference.

B. Random coincidence backgrounds

Signals corresponding to times t_0 , t_f , and t_n were assembled offline into coincidence pairs $\{t_0, t_f\}$ and $\{t_0, t_n\}$, and subsequently into pairs of t_f and t_n that were in coincidence with a common t_0 signal, $\{t_f, t_n; t_0\}$, the latter of which is referred to as a “double coincidence.” Creation of coincidences in this manner provided the division of outgoing neutron energies as a function of incident neutron energy, while also allowing for determination of the time-dependent random coincidence background according to the method described in Ref. [39]. In short, the rate of random (background) coincidences, r_b , for a coincidence measurement between detectors i and j , is described by the product of detection rates, r_i and r_j , and the coincidence window width, Δ_t , i.e.,

$$r_b = r_i r_j \Delta_t. \quad (1)$$

In practice for the present experiment, r_i and r_j are the PPAC fission rate, r_f , and either the Li-glass or liquid scintillator neutron detection rate, r_n . Equation (1) can then be rewritten in terms of background counts, b , as

$$b = r_f r_n n_t \Delta_t^2, \quad (2)$$

with n_t as the number of t_0 signals, which is equivalent to the number of micropulses in the experiment. Given that this method is carried out *in the experimental configuration* (no separate background measurement required) it was shown that the neutron beam can be used a factor of 4 as efficiently compared to an experiment that separately acquired the same statistical precision on the experimental data and random coincidence background. See Ref. [39] for a fully detailed description of this random-coincidence background method.

While the statistical uncertainties of this method are negligible [39], a systematic error can be present in the random coincidence background if rates change during the course of an experiment. There are two primary sources of rate changes during an experiment: predictable and unpredictable changes.

Unpredictable rate changes are the result of, for example, changes in beam intensity or changes in the amount neutrons scattered from other flight paths to a Chi-Nu experiment, among other sources. The only source of a predictable (i.e., well understood) rate change is the WNR beam structure. The 800-MeV proton beam is delivered to the WNR spallation target in “micropulses” 150 ps wide and separated from neighboring micropulses by $\approx 1.8 \mu\text{s}$. Nominally, approximately 347 micropulses are contained within a larger beam pulse called a “macropulse,” and macropulses are delivered to WNR at an average rate of 100 s^{-1} . As micropulses of beam are delivered within a macropulse, beam intensity increases over the first 10–20 micropulses before reaching a plateau, which changes both the PPAC and neutron detector rates, but this was avoided in data analysis by eliminating the first 100 μs of each macropulse for both Li-glass and liquid scintillator data sets. Additionally, as neutrons from the beam and also PFNS neutrons scatter off objects in the experimental environment, an ambient source of epithermal neutrons builds up within the flight path. This buildup increases the neutron detector rate as a function of time within a macropulse but does not alter the PPAC rates appreciably. While the unpredictable rate changes produce a systematic error in the background that is difficult to quantify, the predictable rate changes produce a noticeable deficit in the background with respect to the measured data that must be corrected.

The remainder of this section describes methods to quantify and correct for systematic uncertainties and errors in the random coincidence background. Many of these details will be described further in a forthcoming paper. However, we will include all necessary details in this work because much of the analysis in the rest of this section is presented here for the first time. We will first address the background error from the macropulse structure in Sec. II B 1 and systematic uncertainties from rates changes over the course of the experiment in Sec. II B 2.

1. Background error from macropulse structure

The macropulse structure impacted the low outgoing energy Li-glass results to a much greater extent than the liquid scintillator results. This effect can be corrected by using a simple method: Shift the PPAC timing by 1 micropulse in either direction. This shift should result in a spectrum of measured data that is entirely background since there are no true $\{t_f, t_n\}$ coincidences, i.e., the data and background (d and b) from shifting the PPAC up (d_u and b_u) or down (d_d and b_d) in time should be equal. However, an offset can be observed between the data and background for shifts in either direction. Furthermore, this offset is nearly identical for shifts in either direction, *and* this offset appears to align well with the apparent background deficit in the Li-glass results with all detectors properly aligned in time. Although no apparent deficit existed in the liquid scintillator results, application of this procedure produced a small correction to the measured background. Therefore, the total background, b , for both the Li-glass and liquid scintillator data was determined to be

$$b = b_o + \frac{1}{2}[(d_u - b_u) + (d_d - b_d)], \quad (3)$$

where b_o is the random coincidence background determined by the methods of Ref. [39] with the PPAC and neutron detectors aligned in time. The term within square brackets is the average background deficit with the PPAC shifted up or down by one micropulse and is only applicable to the analysis with no shift if rates vary linearly with time for any set of three micropulses within a macropulse. Note that this term is not itself a background, but only a modification to the aligned background, b_o . While the overall rate of neutron detection varies nonlinearly over the course of a macropulse (see Sec. III A), it can be shown that any set of three micropulses in a macropulse do indeed vary linearly with time to within 0.064% within a Li-glass experiment and to within $\leq 0.001\%$ for a liquid scintillator experiment. Therefore, a systematic uncertainty of 0.064% was applied to the term within square brackets in Eq. (3) for the Li-glass analysis, as described in the uncertainty analysis in Sec. III B, and was ignored for the liquid scintillator analysis (see Sec. IV B).

2. Systematic uncertainty from random rate changes

Random rate changes over the course of an experiment also impacted the background assessment for data collected with both neutron detector arrays. Typically, the data for an experiment are summed together before they are analyzed for the random coincidence background, which based on Eq. (2) yields the background spectrum

$$b = N_R \langle r_f \rangle \langle r_n \rangle \langle n_t \rangle \Delta_t^2, \quad (4)$$

where N_R is the total of number of individual data “runs” and the $\langle \rangle$ brackets indicate averages over the course of all runs of the quantity inside. Alternatively, if the background was calculated for each run before summing all of the data together, then this random coincidence background would be written as

$$b' = N_R \langle r_f r_n n_t \rangle \Delta_t^2. \quad (5)$$

If r_f , r_n , and n_t are all constant, then Eqs. (4) and (5) yield the same background spectrum, but in reality these values can change from run to run. Therefore, Eqs. (4) and (5) are not generally equivalent. However, assuming a consistent spectrum after the formation of each $\{t_f, t_n; t_0\}$ double coincidence, the ratio of Eqs. (4) and (5) should be approximately equal to the ratio of the background spectra after double coincidence formation, i.e.,

$$\frac{b}{b'} = \frac{N_R \langle r_f \rangle \langle r_n \rangle \langle n_t \rangle \Delta_t^2}{N_R \langle r_f r_n n_t \rangle \Delta_t^2} = \frac{\langle r_f \rangle \langle r_n \rangle \langle n_t \rangle}{\langle r_f r_n n_t \rangle}. \quad (6)$$

This ratio was calculated according to the r_f , r_n , and n_t values observed over the course of both Li-glass and liquid scintillator experiments. Given that the treatment of Eq. (5) is more correct in that it eliminates errors from run-to-run rate variations, Eq. (6) might be initially interpreted as a correction factor for the background from Eq. (4). However, although runs were rejected from both the Li-glass and liquid scintillator data sets if outlying values of r_n , r_f , or n_t were observed, these quantities are also changing during the course of each run just as they do from run to run. Thus, this ratio is interpreted as a systematic uncertainty on the background

instead of systematic error correction. These uncertainties are quantified for data collected with both neutron detector array in Secs. III B and IV B.

C. MCNP simulations

It is common in neutron detection experiments to attempt a measurement of the neutron detector efficiency with a calibration source, such as a ^{252}Cf spontaneous fission source (see Ref. [11] and references therein). Alternatively, the efficiency is sometimes determined via computer programs like SCINFUL [20,40–43] or measured via reference resonances or transmission spectrum measurements [44]. All of these methods assume that the chosen neutron detectors have a single efficiency curve, similar to usual treatments of γ -ray detectors. However, the quantity that would be termed the “neutron detection efficiency” depends heavily on the experimental environment because of the high cumulative probability for neutrons to scatter within the experimental environment before detection. The scattering of neutrons leads to “down-scattering,” the process through which neutrons appear at a lower energy because of scattering in the environment. This effect is typically used to describe two separate, but usually indistinguishable experimental mechanisms: physical loss of energy via scattering in the environment and total path length increase. Both effects increase the amount of time it takes for a neutron to travel to the detector and therefore decrease the inferred energy calculated from neutron time of flight.

In efficiency measurements using the $^{252}\text{Cf}(\text{sf})$ PFNS, the measured counts are divided by the $^{252}\text{Cf}(\text{sf})$ PFNS value at the *time-of-flight energy* to determine a relative number of counts expected for a given value of the PFNS. This correction includes both the intrinsic neutron detection efficiency and scattering corrections, but two issues arise from this approach. First, if the experimental environment is changed from that of the $^{252}\text{Cf}(\text{sf})$ measurement, then the interactions of neutrons with the environment change, and the altered contributions to each measured time-of-flight energy from scattering follows. This would happen if, for example, the target was switched to the isotope of interest. Even if the target components and geometries are kept as identical as possible between the ^{252}Cf and another other isotope, there could still be effects that change what would be the correct detector efficiency curve. Second, and more importantly, the efficiency inferred from the $^{252}\text{Cf}(\text{sf})$ PFNS is only appropriate for a measurement of the $^{252}\text{Cf}(\text{sf})$ PFNS. Any change in the PFNS emitted from the target changes the relative number of counts in each bin that are from neutrons of the measured time-of-flight energy to those that are from downscattering. Therefore, the efficiency from a $^{252}\text{Cf}(\text{sf})$ measurement (effectively in units of counts per PFNS value) is only an approximation when used in a measurement of any other PFNS shape, especially considering the wide variety of shapes that can result from neutron-induced PFNS measurements across orders of magnitude of neutron energy. The complication from this fact is that there is no way to know how to properly correct a measurement of a PFNS without first knowing the PFNS itself. The same statements also apply to efficiency curves generated from the other

methods mentioned above that are applied to measurements of various PFNS shapes in different environments.

To address this complicated issue, we have adopted an analysis that employs highly detailed and customized MCNP [45] simulations including essentially every aspect of the experiment environment as well as detector response properties such as time resolution, pulse height resolution, and other effects to account for neutron scattering for each experiment. Historically, MCNP X-PoliMi [46,47] simulations have been validated with $^{252}\text{Cf}(\text{sf})$ measurements using a PPAC with an identical internal construction as the ^{239}Pu shown in this work [48,49]; these simulations have been used for data analysis and PFNS extraction, though more complex issues have recently been addressed via MCNP6 [50] and the PTRAC output format [51–54] (see Secs. II D and III B). We have also attempted to reduce the impact of neutron scattering in a number of ways, including the creation of a 2-m-deep “get-lost basement” below the experimental area to reduce scattering from the floor.

In addition to the detailed studies of neutron scattering effects from experimental environments carried out for the Chi-Nu experiment, the assumptions of scattering corrections required for past experiments have also been challenged. These studies yielded altered interpretations of the literature results that significantly influenced how literature data were treated in PFNS evaluations [12,49,55]. Despite these efforts, scattering still exists within the Chi-Nu experimental environment and the use of MCNP simulations to extract the measured PFNS shape from the experimental data (see Sec. II E) still requires *a priori* knowledge of the measured PFNS. However, the use of simulations to extract the underlying PFNS instead of a measured reference affords the experimenter an important capability that is not otherwise available: the ability to assign a systematic uncertainty on the accuracy of the result. Within simulation, the reference PFNS can be changed over a range of potential PFNS shapes, each of which produces a slightly different result because of scattering within the environment, and the spread in these results can be used to assign this systematic uncertainty. It is this last step that is missing from efficiency measurements in previous works with ^{252}Cf and other similar methods.

D. PPAC angular efficiency and fission fragment anisotropies

The fission-fragment detection efficiency of the PPAC used in these experiments is known to depend on the angle of emission of the fission fragment with respect to the target foil and is also believed to be sensitive to the fragment mass to a lesser extent [31,56]. The natural course for measuring the angular efficiency of the PPAC would be to measure the number of fragments detected as a function of fragment angle for an isotropic source. Unfortunately, the observed PPAC signal has effectively no angular information and so the fission fragment angle cannot be correlated with fragment detection, thereby making a direct measurement of the PPAC angular detection efficiency impossible. However, the kinematics of neutrons emitted from fission fragments is such that the highest-energy neutrons observed in a given neutron detector are from fragments that are emitted directly toward

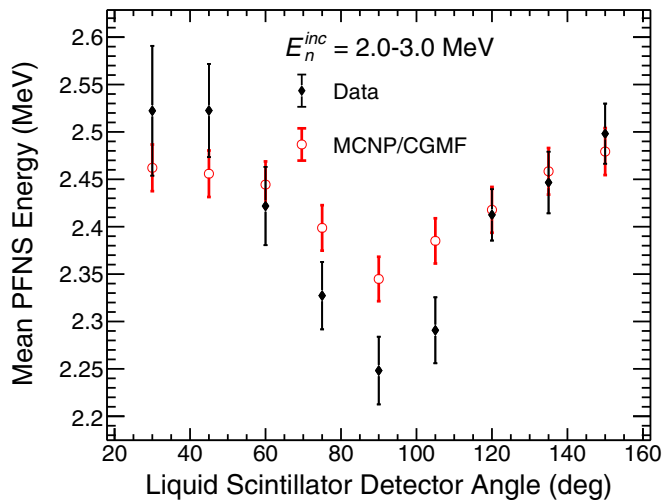


FIG. 5. The mean PFNS energy as a function of laboratory detection angle with respect to the incident neutron beam for the incident energy of $E_n^{\text{inc}} = 2\text{--}3$ MeV is shown here for the present measurement (black diamonds) and the corresponding MCNP6 simulation (red circles). For this incident neutron energy bin the fragments are emitted close to isotropically in the center-of-mass frame and there is very little motion of the center of mass. Therefore, the pattern observed in this figure is primarily a result of the PPAC angular efficiency. See the text for a discussion.

that detector. It follows that the PFNS observed at angles corresponding to a *lower* fragment detection efficiency should be *softer* (i.e., fewer high-energy neutrons and therefore a lower mean spectrum energy). As a corollary to this statement, the detectors perpendicular to lower-fragment-efficiency angles will observe a harder spectrum. Indeed, this is precisely what is observed for the ^{239}Pu PFNS as a function of angle, an example of which is shown in Fig. 5 as the black diamonds.

A connection must be made between the unmeasured fission fragment angles and the measured time-of-flight neutron energies to address the issue of an unknown PPAC angular efficiency. To accomplish this task, calculations of ^{239}Pu neutron-induced fission for 1 MeV increments from $E_n^{\text{inc}} = 1\text{--}20$ MeV were carried out with the CGMF code [5] to generate distributions of the emitted neutron energies and angles corresponding to each fragments angle and for each incident energy. Separately, MCNP6 simulations of neutrons leaving each PPAC target were analyzed with the PTRAC [51] output format to create distributions of emitted (initial) neutron energies and angles as a function of measured neutron time-of-flight energies and detector angles. Finally, for each measured neutron energy and angle within the simulation, the corresponding initial neutron energy and angle was used to increment a total probability distribution for the fission fragment angle that could have created the detected neutron. An example of this distribution is shown in Fig. 6 after integrating over all measured neutron angles in simulation.

The distribution in Fig. 6 can now have a weighting function, i.e., a PPAC angular efficiency curve, applied to the different fragment emission angles. The simulation spectrum associated with the chosen efficiency curve is then the y-axis

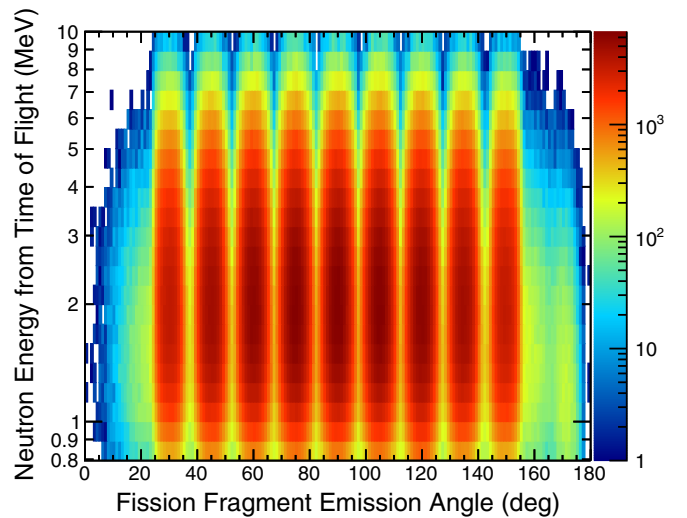


FIG. 6. The distribution of neutron energies from time of flight as a function of fragment emission angle generated via the methods described in Sec. II D.

projection of Fig. 6. The mean energy trend as a function of angle shown in Fig. 5 was used as guidance for the accuracy of the applied efficiency curve. For the purposes of this work, efficiency curves were varied manually to arrive at a reasonable estimate of the PPAC angular efficiency such that the effect of this efficiency could be studied. The result of these variations is shown as the red circles in the same figure. The efficiency curve itself was assigned a 10% uncertainty across all fragment angles, and this was used to estimate the covariance associated with the PPAC angular efficiency described in Sec. IV B. While the MCNP/CGMF reproduction of this pattern of mean energy as a function of neutron detection angle is not within $1\text{-}\sigma$ agreement at the angles near 90° , by design of the Chi-Nu experiment [57] the angle-integrated result of data from each detector angle is similar to the input PFNS spectrum for the simulation, implying that this source of systematic error and uncertainty has a minimal impact on the PFNS results. Nonetheless, more sophisticated methods for reproducing this feature of the measured data will be investigated in future work.

The CGMF code was also used to study the possibility of a bias in our PFNS results from kinematic effects and from fission fragment anisotropies [58,59]. CGMF calculates the kinematic effects on fragments and the emitted neutrons and includes fission fragment anisotropies using the result of a fit to literature fragment anisotropy data [60–65]. The impact of the total fragment anisotropy (the combination of kinematics and intrinsic fragment anisotropies) was tested by generating probability distributions of the total fragment anisotropy as a function of incident energy for multiple incident energies from 1–20 MeV. These distributions were used as a weighting for the distribution shown in Fig. 6 and compared to the result with no kinematics or fragment anisotropies. This method is analogous to that used to test the impact of the PPAC angular efficiency. The largest impact observed from these effects was a change by 0.22 keV ($\approx 0.009\%$) on the average PFNS energy. Given the small size of this effect, fragment anisotropies

and kinematics were disregarded for the uncertainty analysis in this work. The PPAC angular efficiency was the dominant source of uncertainty relating to fission fragment emission and detection.

E. The ratio-of-ratios method

The ratio-of-ratios method [49] was used to generate the PFNS results shown in this work. The general form of the unnormalized ratio-of-ratios expression is

$$p_i = \frac{d_i - b_i}{F_i}, \quad (7)$$

where the subscript, i , refers to the PFNS energy, E_i , at which the PFNS data point, p_i , is reported. Energy bins were chosen at 20 bins per decade of neutron energy to ensure sufficient statistical precision for each energy bin. The parameters d , b , and F are the measured counts in the data from either the Li-glass or liquid scintillator detectors, the background calculated according to Sec. II B, and the correction factor for detector efficiency and environmental scattering, respectively. The F factor is calculated using MCNP simulation spectra generated using the environmental detector response matrix formalism used at Chi-Nu [66,67], and the response matrix itself was calculated with MCNP X-PoliMi [46] including time resolution, pulse-height resolution, and other relevant features of the detector response [49]. The F correction factor is described by

$$F_i = \frac{1}{\nu} \sum_{\pi=1}^{\nu} \frac{c_{\pi,i}}{p_{\pi,i}}, \quad (8)$$

where the index π denotes a unique PFNS distribution, $p_{\pi,i}$ is the PFNS, p_{π} , evaluated at E_i , and $c_{\pi,i}$ is the counts from a simulation carried out with PFNS p_{π} in the bin corresponding to energy E_i . The F_i sum is over ν different PFNS distributions, chosen to vary widely enough such that they are likely to contain the desired ^{239}Pu PFNS. These distributions are the following:

- (1) Watt spectrum with $a = 0.988$ MeV and $b = 2.249$ MeV $^{-1}$ (to resemble a ^{235}U PFNS),
- (2) Watt spectrum with $a = 0.966$ MeV and $b = 2.842$ MeV $^{-1}$ (to resemble a ^{239}Pu PFNS),
- (3) Watt spectrum with $a = 1.025$ MeV and $b = 2.926$ MeV $^{-1}$ (to resemble a ^{252}Cf PFNS),
- (4) The $^{252}\text{Cf}(sf)$ evaluation of Ref. [68],
- (5) A low-incident-energy ^{239}Pu PFNS from ENDF/B-VII.1 [14].

See Eq. (31) for the Watt spectrum functional form. This parameter corrects for neutron detection physics (i.e., intrinsic detection efficiency) and multiple-scattering effects by calculating the average ratio of the measured foreground counts to the true underlying PFNS distribution. However, neutrons of different initial energies interact differently with the experimental environment, and so this ratio is not a constant for all p_{π} , which will result in a systematic uncertainty described in Secs. III B and IV B. PFNS shapes were calculated separately for both the Li-glass and liquid scintillator data sets and then combined as described in Sec. V.

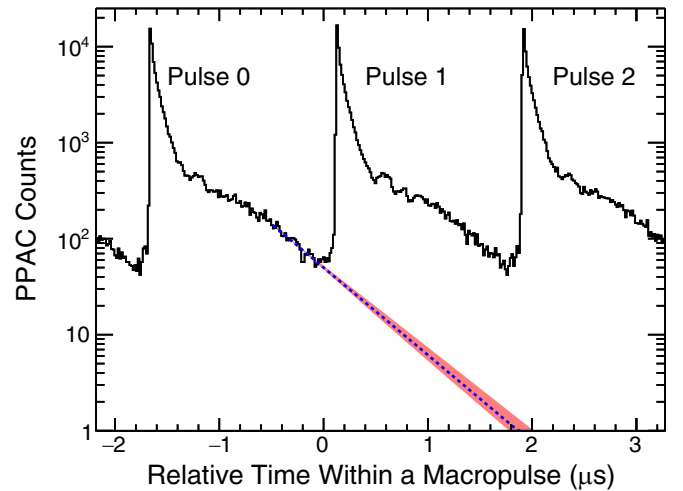


FIG. 7. An example spectrum of the number of fissions observed as a function of time within a macropulse for three micropulses. See the text for a description of the two varieties of wraparound. The exponential extrapolation of the low-energy wraparound is shown as the blue dashed line with the uncertainty band shown as the shaded region. The relative time is defined such that pulse 1 begins at approximately 0 μs .

F. Wraparound corrections to the PFNS results

A correction was made to the PFNS results shown here for the “wraparound” effect. We will first briefly describe the origin of this effect: experiments using pulsed, white sources of incident neutrons are subject to effects amounting to contamination of the assumed incident neutron spectrum from neighboring incident neutron pulses. In fact, there are two effects that could be termed as wraparound, which we will call high- and low-energy wraparound. High-energy wraparound occurs when the high-energy neutrons from the next pulse arrive at a detector (the PPAC, in this case) at a time corresponding to slower neutrons from the present pulse. High-energy wraparound is shown in Fig. 7 as pulse 2 contaminating pulse 1 at approximately 1.8 μs . In practice, this effect can be identified because, among other things, the incident neutron flux sharply increases as the next pulse arrives, and so the entire issue is avoided by placing a lower limit on the reported incident neutron energies. It is the high-energy wraparound effect that drives the low-energy threshold of $E_n^{\text{inc}} = 1$ MeV for this work.

On the other hand, low-energy wraparound occurs when low-energy incident neutrons from the previous pulse arrive at the detector at a time corresponding to higher energies from the present pulse. Low-energy wraparound is demonstrated in Fig. 7 as the low-energy neutrons from pulse 0 contaminating pulse 1. In principle, the low-energy neutrons from pulse 0 and every other preceding pulse also contaminate the inferred incident neutron spectrum in an analogous way, but contaminations from additional pulses are negligible. This effect is more difficult to quantify, it cannot be cleanly removed from the data, and a correction must instead be applied to the PFNS results based on the incident neutron flux pattern. The treatment of low-energy wraparound is the focus of this

section. This treatment is split into two parts: the fractional contamination of the counts measured at each incident neutron energy (i.e., the fraction of the counts at each incident energy from wraparound) and the shape of the contaminant PFNS from the wraparound incident neutrons. These effects and their associated covariance derivations are discussed in Secs. [II F 1](#) and [II F 2](#), respectively, and the total correction applied to the data is described in Sec. [II F 3](#).

1. Low-energy wraparound contamination fraction

The wraparound contamination fraction can be estimated by looking at the number of fissions detected as a function of time within a macropulse, as is shown in Fig. 7. The low-energy (long-time) tail of pulse 0 is fit with an exponential assuming a diagonal statistical covariance matrix for the counts shown in Fig. 7, and the extrapolation of this fit into pulse 1 is used to estimate the low-energy wraparound contamination. The centroid result of the fit is shown in Fig. 7 as the dashed line, and the shaded region shows the $1\text{-}\sigma$ uncertainty band on the fit derived by a Monte Carlo sampling of the covariance from the exponential fit. For each time bin within the incident energy range of interest for pulse 1 ($E_n^{\text{inc}} = 1\text{--}20$ MeV corresponds to approximately $0.281\text{--}1.484$ μs) the exponential fit in Fig. 7 estimates the low-energy wraparound contamination fraction, $x(t)$, defined by

$$x(t) = \frac{e(t)}{c(t)}, \quad (9)$$

where $e(t)$ and $c(t)$ are the exponential fit and counts at time t , respectively. The covariance matrix for $x(t)$ is derived from the diagonal $c(t)$ covariance matrix and the nondiagonal $e(t)$ covariance matrix. The $e(t)$ covariance matrix is output from the fit in parameter space and is converted to time space before use in the $x(t)$ covariance matrix. There is no covariance between $e(t)$ and $c(t)$. Thus,

$$\text{cov}[x(t)]_{ij} = x(t_i)x(t_j) \left\{ \frac{\text{cov}[e(t)]_{ij}}{e(t_i)e(t_j)} + \frac{\delta_{ij}\text{cov}[c(t)]_{ij}}{c(t_i)c(t_j)} \right\}, \quad (10)$$

$$= x(t_i)x(t_j) \left\{ \frac{\text{cov}[e(t)]_{ij}}{e(t_i)e(t_j)} + \frac{\delta_{ij}}{c(t_i)} \right\}, \quad (11)$$

where δ_{ij} is a Kronecker δ function for time bins i and j . Rather than convert these contamination fractions to energy space and apply them individually to each incident energy range, an average contamination fraction, \bar{x} , was calculated as

$$\bar{x} = \frac{1}{N_t} \sum_{i=1}^{N_t} x(t_i), \quad (12)$$

where N_t is the total number of time bins considered and

$$\text{var}[\bar{x}] = \sum_{k=1}^{N_t} \sum_{l=1}^{N_t} \left[\frac{\partial \bar{x}}{\partial x(t_k)} \right] \text{cov}[x(t)]_{kl} \left[\frac{\partial \bar{x}}{\partial x(t_l)} \right], \quad (13)$$

$$= \sum_{k=1}^{N_t} \sum_{l=1}^{N_t} \frac{\text{cov}[x(t)]_{kl}}{N_t^2}. \quad (14)$$

The average contamination fraction resulting from this procedure was $\bar{x} = 0.0290(49)$, and it is this value that was assumed for the low-energy wraparound correction.

It should be noted that the spectrum in Fig. 7 corresponds to the number of fissions as a function of time within a macropulse *after* forming coincidences between measured t_0 , fission, and neutron signals and also after application of additional gates to select neutrons from the acquired data (see Secs. [III A](#) and [IV A](#)). Therefore, the spectrum in Fig. 7 corresponds only to counts that made it through to the final result, which is the appropriate quantity for this correction. While it might be assumed that the same answer should result if the contamination fraction was estimated with the counts in the equivalent spectrum of Fig. 7 *before* these additional analysis steps, the contamination fraction would actually be $0.0734(37)$ in this case. The most obvious reason for this change in the contamination fraction is that $\bar{\nu}(E_n^{\text{inc}})$, the average number of neutrons emitted per fission, increases with increasing incident neutron energy, and so there are more opportunities for detecting a neutron in coincidence with a measured fission. However, ignoring the important effects of the energy dependence of the neutron detection efficiency and changes in PFNS spectrum as a function of incident neutron energy, this effect should only account for a decrease in \bar{x} by $\bar{\nu}(E_n^{\text{inc}})/\bar{\nu}(E_n^{\text{inc}})$, where E_n^{inc} corresponds to the wraparound incident neutron energy. At most, this should decrease \bar{x} from 0.0734 to approximately 0.0423 based on the $\bar{\nu}(E_n^{\text{inc}}) \approx 5$ and $\bar{\nu}(E_n^{\text{inc}}) \approx 3$ for $E_n^{\text{inc}} = 20$ MeV with a smaller change expected for lower incident neutron energies [[69–72](#)]. The further reduction in \bar{x} results from the analysis described in Secs. [III A](#) and [IV A](#) and is likely the result of data reduction from coincidence analysis and gating. Regardless of the reasons behind the measured \bar{x} after analysis of the spectra from each detector type, the number of fissions that reach the final analysis (i.e., those shown in Fig. 7) is the relevant quantity for correcting the PFNS results for the low-energy wraparound effect.

2. Wraparound contaminant PFNS shape

Considerations of the PFNS shape corresponding to the low-energy wraparound incident neutrons requires careful thought. The most obvious issue with defining this shape is that the wraparound energy corresponding to each incident energy is unique. The wraparound energy ranges from 0.215 MeV at $E_n^{\text{inc}} = 1$ MeV to 0.522 MeV at $E_n^{\text{inc}} = 20$ MeV, and so the shape of the low-energy wraparound PFNS changes as a function of the measured incident neutron energy. The natural choices for characterizing this wraparound PFNS shape would be either a measurement of the PFNS at these energies or an evaluation PFNS at the wraparound energies. Unfortunately, the high-energy wraparound prevents the PFNS at the wraparound energies from being reported in this work. Alternatively, a reasonable approximation might be to extrapolate a nuclear data evaluation such as ENDF/B-VIII.0 [[15](#)] to the correct wraparound energy for each measured incident neutron energy. However, this choice is also not ideal because, as will be shown in Sec. [VI](#), the results presented here do not perfectly agree with ENDF/B-VIII.0 or any other

nuclear data evaluation, which implies that choosing one of these evaluations would inappropriately bias the results toward the chosen evaluation. For these reasons the lowest incident energy PFNS reported in this work was used to characterize the low-energy wraparound PFNS shape. This choice is supported by two observations made when quantifying the wraparound correction: (1) the correction made to the lowest incident neutron energy PFNS spectrum reported here assuming the $E_n^{\text{inc}} = 500$ keV ENDF/B-VIII.0 PFNS is essentially negligible, and (2) the correction to the PFNS shapes at higher incident neutron energies in this work is similar to that calculated when using the ENDF/B-VIII.0 PFNS at $E_n^{\text{inc}} = 500$ keV, both of which suggests that the lowest incident energy PFNS reported here is sufficient for this correction. An additional advantage of this approach is that the data analysis is self-contained and does not rely on the use of some particular evaluation that happens to be available today.

Rather than directly using the measured PFNS at the lowest reported incident energy to correct the PFNS shapes at all higher incident energies, thereby propagating statistical fluctuations, a Watt spectrum [2,3] fit was performed instead, and the result of this fit was used as the shape of the wraparound contaminant PFNS. This fit to the PFNS at $E_n^{\text{inc}} = 1.0\text{--}2.0$ MeV included the complete experimental covariance matrix of the PFNS before corrections for the low-energy wraparound effect, and the overall scaling of the Watt function was defined at each iteration rather than being included as an additional fit parameter. Both of these features of the fit were incorporated via the TMinuit class [73] of the ROOT data analysis framework [74]. The fit resulted in the Watt parameters $a = 1.0464(36)$ and $b = 2.258(35)$ with a parameter correlation of -0.614 . Again, see Eq. (31) for the Watt spectrum functional form. The parameter covariance was converted to an energy-space covariance matrix binned exactly as the PFNS data.

3. Application of the low-energy wraparound correction

The low-energy wraparound correction was applied to the PFNS points, p_i , at all but the lowest incident neutron energy (since this was used to derive the wraparound contaminant PFNS shape) using the relation

$$p'_i = \frac{p_i - \bar{x}W_i}{1 - \bar{x}}, \quad (15)$$

where W_i is the value of the Watt spectrum wraparound fit at PFNS energy E_i , \bar{x} is the average wraparound contamination factor described in Eq. (12), and p'_i is the wraparound-corrected PFNS value at the same PFNS energy. Note that this correction is applied to the PFNS data before the combination of different detectors and normalization described in Sec. V. However, this correction requires that the unnormalized PFNS data be scaled such that the centroids are in the same relative position as in the normalized PFNS. Thus, the area of both the unnormalized PFNS and the Watt function is equal to unity and including the $1 - \bar{x}$ term in the denominator preserves this area for the wraparound-corrected PFNS. The covariance of

the wraparound-corrected PFNS is

$$\begin{aligned} \text{cov}[p']_{ij} &= \frac{\partial p'_i}{\partial p_i} \text{cov}[p]_{ij} \frac{\partial p'_j}{\partial p_j} + \frac{\partial p'_i}{\partial W_i} \text{cov}[W]_{ij} \frac{\partial p'_j}{\partial W_j} \\ &+ \frac{\partial p'_i}{\partial \bar{x}} \text{var}[\bar{x}] \frac{\partial p'_j}{\partial \bar{x}}, \end{aligned} \quad (16)$$

$$\begin{aligned} &= \frac{\text{cov}[p]_{ij}}{(1 - \bar{x})^2} + \frac{\bar{x}^2 \text{cov}[W]_{ij}}{(1 - \bar{x})^2} \\ &+ \text{var}[\bar{x}] \left[\frac{p_i - \bar{x}W_i}{(1 - \bar{x})^2} - \frac{W_i}{(1 - \bar{x})} \right] \\ &\times \left[\frac{p_j - \bar{x}W_j}{(1 - \bar{x})^2} - \frac{W_j}{(1 - \bar{x})} \right]. \end{aligned} \quad (17)$$

The uncertainty analyses described in Secs. III B and IV B are contained within the $\text{cov}[p]$ term, and the data discussed in Sec. V have been corrected in this manner for the low-energy wraparound effect. In this work, this is the only source of uncertainty correlating the Li-glass and liquid scintillator data sets prior to the normalization procedure described in Sec. V.

III. Li-GLASS ANALYSIS

A. Data analysis

Neutron detection in ${}^6\text{Li}$ -glass detectors proceeds via the ${}^6\text{Li}(n, t)$ reaction, which has a Q value of 4.784 MeV, a resonance at approximately 240 keV, and is a standard up through 1 MeV [15,75]. All of these features make neutron detection via ${}^6\text{Li}(n, t)$ attractive for low-energy neutrons. However, the large thermal cross section for the ${}^6\text{Li}(n, t)$ reaction also makes these detectors especially susceptible to the buildup of epithermal neutrons in the experimental flight path area, as described in Sec. II B. An example of the number of neutrons detected in a ${}^6\text{Li}$ -glass detector (including background neutrons) as a function of time within the macropulse is shown in Fig. 8. The Li-glass rate change shown in Fig. 8 required the use of the methods described in Sec. II B in order to correctly determine the random coincidence background for Li-glass data.

Neutrons determined to be part of a valid double coincidence are processed in terms of neutron kinematics from the PPAC to the Li-glass detector. An example kinematic spectrum for ${}^6\text{Li}$ -glass detectors is shown in the top panel of Fig. 9. The region within the solid (red) kinematic gate contains neutrons along the expected kinematic curve for neutrons traveling from the PPAC to a neutron detector. The counts within the vertical line at $t_n - t_f = 0$ ns correspond to fission γ rays, the parallel vertical band at $t_n - t_f \approx 10$ ns corresponds to other reactions within the glass, and the horizontal band at 0.1 V μs contains both low-energy fission neutrons and the random coincidences formed by epithermal neutrons. The counts within the kinematic gate in the top panel of Fig. 9 are converted to outgoing neutron energy via time of flight. This spectrum is shown in the bottom panel of Fig. 9 for an incident neutron energy of $E_n^{\text{inc}} = 2.0\text{--}3.0$ MeV (corresponding to an average incident energy of $\langle E_n^{\text{inc}} \rangle = 2.514$ MeV) with the random coincidence background determined according to Ref. [39]. The bump in this spectrum at $E_t = 240$ keV is from

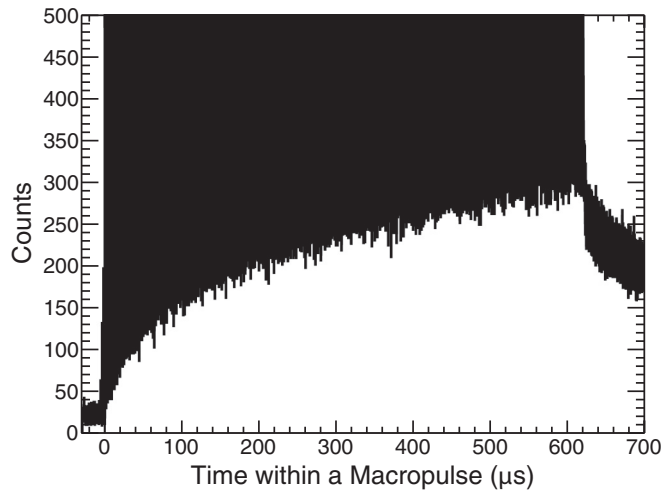


FIG. 8. Number of neutron detections as a function of time within a macropulse for a ^6Li -glass detector. The y-axis maximum is reduced well below the maximum number of counts to emphasize the changes in neutron detection rate. See the text for a discussion.

the $^6\text{Li}(n, t)$ resonance at approximately the same energy. The measured data spectrum consists of >99% background at the lowest energies.

The Li-glass PFNS results reported in this work were calculated via the method described in Sec. II E using the response matrix methodology described in Ref. [66]. The Chi-Nu Li-glass response matrix with a ^{239}Pu PPAC is shown in Fig. 10. To briefly summarize the details of this matrix discussed in Refs. [52,66], this response matrix describes the interaction between PFNS neutrons and the experimental environment as a function of PFNS neutron energy and the measured time-of-flight neutron energy. Neutrons near the diagonal correspond to neutrons that were emitted from the target and detected in a Li-glass detector with either no scattering or a small number of scatters that did not impact the total time of flight before detection. Every other neutron in this matrix scattered at least once before detection and did so in such a way that significantly extended the neutron time of flight compared to that of the PFNS neutron energy. Note that while this process (downscattering; see Sec. II C) always yields a measured energy that is lower than the desired PFNS energy, it can produce counterintuitive effects that must be understood. For example, as was discussed in Ref. [67], a neutron with an energy just above the 240-keV $^6\text{Li}(n, t)$ resonance energy can reach a detector faster than a neutron at the resonance energy, but then undergo a scattering reaction quickly followed by a capture on the resonance without significantly altering the measured time of flight. This yields an excess of counts above the 240 keV resonance peak observed in the data, which shifts the centroid energy of the observed resonance peak up by 20–30 keV. This specific effect becomes an issue if, for example, the $^6\text{Li}(n, t)$ resonance is used to calibrate the timing of an experiment, as was done in Ref. [44]. Similar effects impact the entire measured neutron spectrum, further emphasizing the fact that the concept of a single neutron detector efficiency is not a reliable concept for neutron detection experiments.

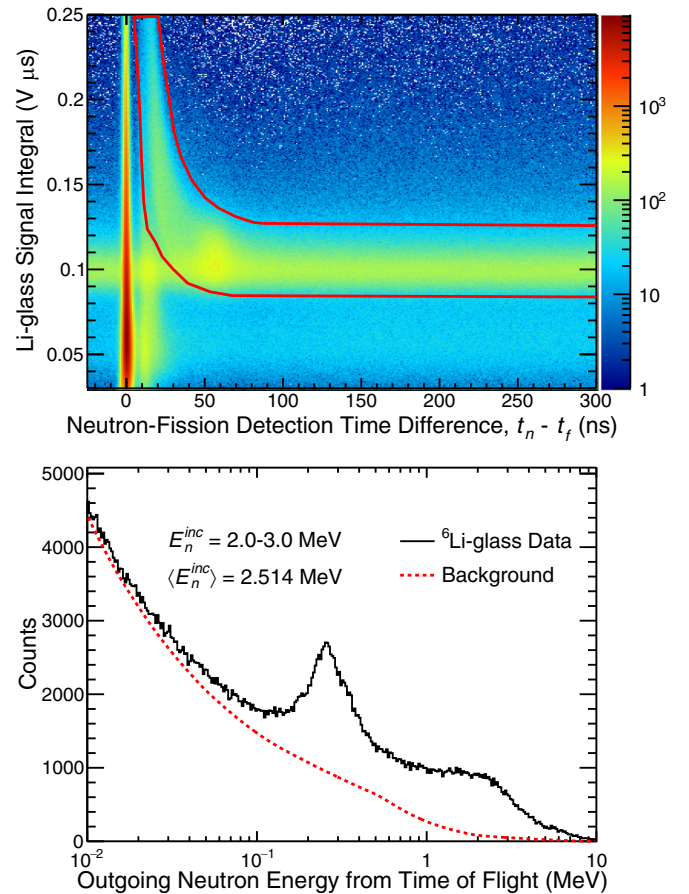


FIG. 9. Top: A kinematic spectrum for neutrons determined to be part of a valid double coincidence. Bottom: A spectrum of the measured data (black, solid line) and the random coincidence background spectrum (red, dashed line) for incident neutron energy $E_n^{\text{inc}} = 2.0\text{--}3.0$ MeV, which corresponds to an average incident energy of $\langle E_n^{\text{inc}} \rangle = 2.514$ MeV. Counts per bin are plotted versus an outgoing neutron energy calculated from the time of flight from the PPAC to the ^6Li -glass neutron detector, assuming a straight-line path. See the text for a discussion of both figures.

B. Uncertainty quantification

While there are only three parameters in Eq. (7), sources of statistical and systematic uncertainty arise from multiple aspects of the analysis. The counts in the raw data spectrum acquired from the experiment, which include both foreground and background, have a simple statistical uncertainty equal to the square root of the counts and no off-diagonal correlations. This diagonal covariance matrix is represented as

$$\text{cov}[d]_{ij} = \delta_{ij}d_i. \quad (18)$$

The δ_{ij} is a Kronecker δ . The values in this matrix represent the statistics of the measured data.

The covariance of the Li-glass background contains both statistical and systematic uncertainties, according to the methods described in Sec. II B. Although the statistical uncertainty on the calculated random coincidence backgrounds is negligibly small [39], there is a statistical component from the data collected when the PPAC detection times are shifted by

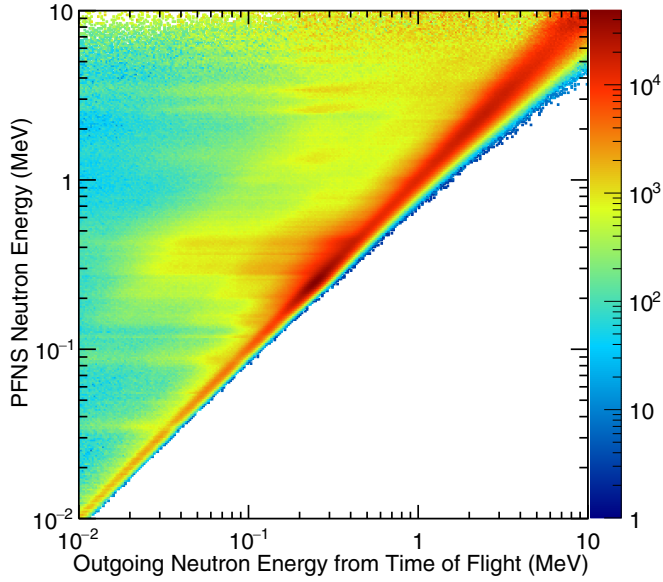


FIG. 10. The Chi-Nu Li-glass response matrix including a ^{239}Pu PPAC is shown here. This matrix was calculated with MCNP X-PoliMi.

one micropulse up and down with respect to the Li-glass neutron detections. Systematic components also arise from both neutron detection rate changes as a function of time within a macropulse and random changes in the fission rate, neutron rate, and number of micropulses in a run. Following Eq. (3), the covariance of the Li-glass background has the form

$$\text{cov}[b]_{ij} = \delta_{ij} \left[\frac{d_u + d_d}{4} \right] + \sigma_{b,r}^2 \left[b_{o,i} b_{o,j} + \sigma_{b,l}^2 \times \left(\frac{b_{u,i} b_{u,j} + b_{d,i} b_{d,j}}{4} \right) \right]. \quad (19)$$

The parameter $\sigma_{b,r}$ is the systematic uncertainty percentage from random rate changes during this Li-glass experiment calculated according to Eq. (6), equal to 0.51% for this data set, and $\sigma_{b,l}$ is the systematic uncertainty associated with the assumption that any three micropulses vary linearly so that Eq. (3) is valid, equal to 0.064% here.

The F multiple-scattering correction factor in Eq. (7) contains both statistical and systematic uncertainties. Statistical uncertainties arise from statistics in the response matrix used to calculate the various simulated spectra and are small compared to the systematic effects. Nonetheless, they are included in the form

$$\text{cov}[F]_{ij,\text{stat}} = \frac{\delta_{ij}}{v^2} \sum_{\alpha}^v \sum_{\beta}^v \sum_{k=1}^n \frac{R_{ik} p_{\alpha k} p_{\beta k}}{p_{\alpha k}^2 p_{\beta k}}. \quad (20)$$

In this equation, p_{α} and p_{β} correspond to the v different PFNS shapes used in the ratio-of-ratios method (see Sec. II E), p_o is the original PFNS shape used as an energy weighting distribution for the response matrix in Fig. 10 (see Ref. [66]), i and j are indices corresponding to the n different time-of-flight measured outgoing energy bins of the simulation, k is an

index corresponding to the initial neutron energy upon leaving the target (i.e., the true PFNS neutron energy), and the R_{ik} are the counts in the response matrix at the bin corresponding to measured neutron energy bin i and initial neutron energy bin k .

Each different PFNS distributions chosen for calculation of F predicts a different multiple-scattering correction, and the spread in these corrections implies a systematic uncertainty in the predicted correction via F . This systematic uncertainty is calculated according to

$$\text{cov}[F]_{ij,\text{syst}} = \frac{1}{v-1} \sum_{\alpha}^v \left(\frac{c_{\alpha i}}{p_{\alpha i}} - F_i \right) \left(\frac{c_{\alpha j}}{p_{\alpha j}} - F_j \right), \quad (21)$$

where $c_{\alpha,i}$ and $c_{\alpha,j}$ are the counts in the simulation (i.e., projection of the response matrix) corresponding to PFNS shape α and outgoing neutron bin i and j , respectively. The spread of these corrections is significant for the Li-glass data, especially at low outgoing neutron energies ($\approx 3-4\%$ at 10 keV), but is smaller for higher-energy neutrons detected with the Li-glass detectors.

The largest additional uncertainty source arising from the MCNP simulation used in this work was determined to be uncertainties in the ${}^6\text{Li}(n, t)$ cross section itself. Despite the fact that this cross section is a standard, it impacts all areas of the measured spectrum in multiple ways, and so this cross section was varied according to its covariance utilizing implicit-capture simulations with MCNP6 and MCNPTools with the PTRAC output format (see Ref. [52] for a full description of this procedure). This additional source of systematic uncertainty was incorporated directly from the results of Ref. [52], and corresponds to the covariance matrix

$$\text{cov}[m]_{ij} = \sigma_{mij}. \quad (22)$$

Note that these uncertainties are applied to the *foreground* counts, i.e., $d - b$, since they apply to the counts acquired from the Monte Carlo. While it is apparent from Fig. 10 that multiple other reactions also impact the measured spectrum [e.g., ${}^{27}\text{Al}(n, n)$, ${}^{16}\text{O}(n, n)$, etc.], the impact of the uncertainty of these reactions on the present results is assumed to be significantly smaller than that of ${}^6\text{Li}(n, t)$ since every detected neutron has to be captured through this reaction. Therefore, these additional sources of systematic uncertainty are ignored for the present results, but could be explored in the future.

Additional sources of uncertainty that were explored for the liquid scintillator detectors but not for the Li-glass detectors are uncertainties relating to the choice of MCNP postprocessing parameters and to the PPAC angular efficiency. Definition of Li-glass MCNP postprocessing parameters such as time resolution, pulse height gain, pulse height resolution, and kinematic gate placement benefit from the existence of the 240-keV resonance in the ${}^6\text{Li}(n, t)\alpha$ reaction. This resonance creates a distinct feature in both the data and simulation that allowed for these parameters to be accurately defined, and the lack of such a feature in the liquid scintillator spectra resulted in the need for an additional systematic uncertainty in the liquid scintillator results. The PPAC angular efficiency systematic was ignored for the Li-glass detectors because, as discussed in Sec. II D, the loss of fragments emitted at certain

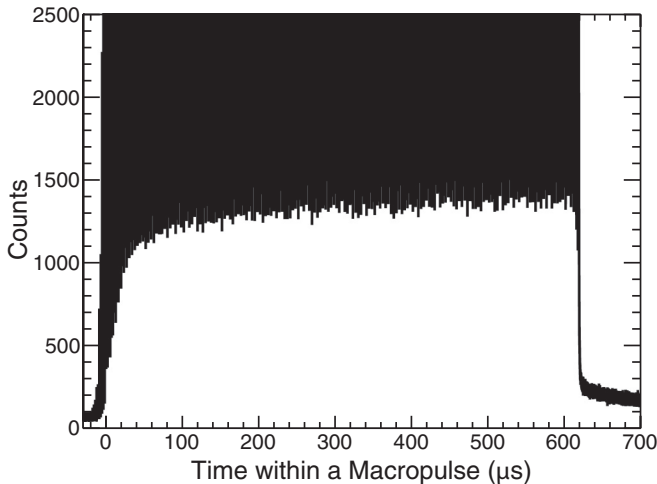


FIG. 11. Number of neutron detections as a function of time within a macropulse for liquid scintillator data. The y-axis maximum is reduced to emphasize the changes in neutron detection rate. See the text for a discussion.

angles primarily causes a loss of the highest-energy neutrons emitted at angles similar to the inefficient fragment detection angles. Given that the Li-glass detectors are measuring low-energy neutrons, this effect is believed to be much smaller than the other uncertainty sources already described in this section.

Propagation of these uncertainties yields the unnormalized Li-glass covariance matrix defined as

$$\text{cov}[p]_{ij} = \frac{1}{F_i F_j} (\text{cov}[d]_{ij} + \text{cov}[b]_{ij} + \text{cov}[m]_{ij} + p_i p_j \text{cov}[F]_{ij}). \quad (23)$$

Examples of this unnormalized covariance matrix are shown in Sec. V alongside similar matrices from the liquid scintillator detectors.

IV. LIQUID SCINTILLATOR ANALYSIS

A. Data analysis

As opposed to Li-glass detectors in which neutrons are *captured* in the detection medium, neutron scattering on hydrogen and carbon are the primary detection reactions for liquid scintillators. Although the dynamic range of these detectors was tuned to provide a reasonable overlap with the Li-glass detectors, these detectors are naturally more sensitive to higher-energy neutrons, and so, in principle, these detectors should be less sensitive to the buildup of epithermal neutrons within the Chi-Nu experimental area. An equivalent plot of Fig. 8 for the liquid scintillator detectors is shown in Fig. 11. Whereas the Li-glass detectors display a nonlinearly increasing baseline of counts over the course of a macropulse, the count rate for the liquid scintillator detectors rises sharply at short times but then becomes nearly constant after approximately $75 \mu\text{s}$, implying that the background corrections for predictable rate changes described in Sec. II B were not necessary.

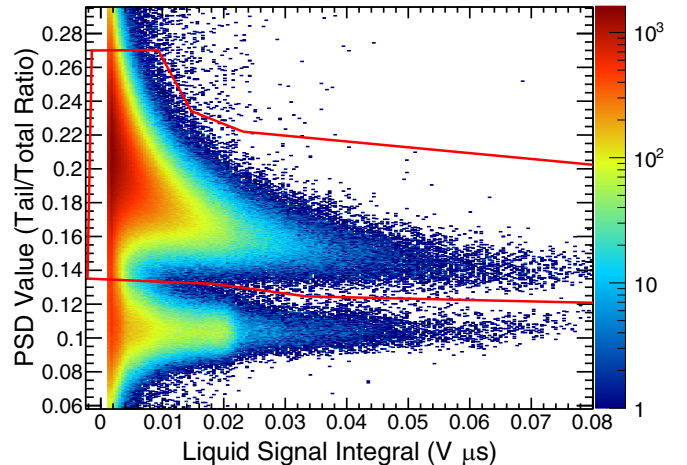


FIG. 12. An example of a liquid scintillator PSD spectrum is shown here. The gate for neutrons is shown as the area bounded by the red line.

In addition to neutrons, liquid scintillator detectors have a nonnegligible efficiency for detecting γ rays. These γ rays are then a potential background for the desired neutrons because the neutron signals are not boosted by a reaction Q value, as is the case with Li-glass detectors. The pulse-shape discrimination (PSD) properties of liquid scintillators and also reaction kinematics were exploited to separate counts from neutrons and γ rays. An example PSD spectrum for Chi-Nu liquid scintillator detectors during this experiment is shown in Fig. 12 with the chosen gate to select on neutrons. The horizontal band of counts below the PSD gate corresponds to γ rays that are excluded from the data analysis. The top panel of Fig. 13 shows an example kinematic spectrum for neutrons traveling from the PPAC to a liquid scintillator with a kinematic gate used to select PFNS neutrons shown in red. The bottom panel of Fig. 13 shows an example spectrum of the acquired data and background for the incident energy range $E_n^{\text{inc}} = 2.0\text{--}3.0 \text{ MeV}$ after application of PSD and kinematic gates.

Following the same procedure described in Sec. III A, the response matrix for the liquid scintillator experimental environment was created with MCNP X-PoliMi simulations and is shown in Fig. 14. Features in this matrix are generally similar to those in Fig. 10, though fewer environment interactions are apparent in the matrix. This is reflective of the fact that counts from the liquid scintillator detectors were less impacted by environmental scatters overall, though clear structures corresponding to various reactions and objects in the experimental environment can be seen. The counts in this matrix were handled identically to the Li-glass analysis to calculate the liquid scintillator PFNS results shown in this work.

B. Uncertainty quantification

Statistical uncertainties on the liquid scintillator data, background, and F multiple-scattering correction factor, as well as the systematic uncertainties on F and the background were handled identically for both the liquid scintillator and Li-glass data. The statistical and systematic contributions to the F

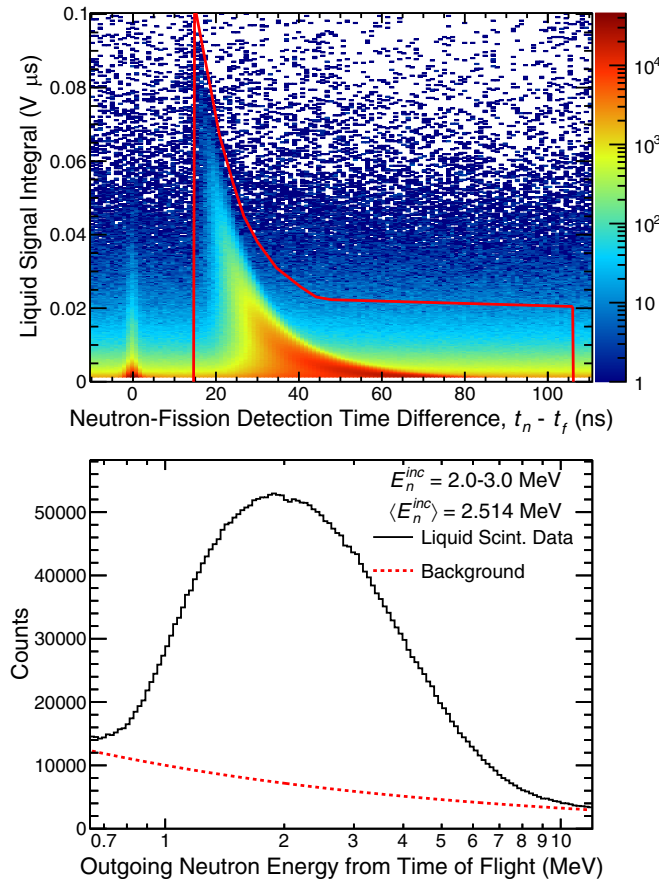


FIG. 13. Top: A kinematic spectrum for neutrons determined to be part of a valid double coincidence. Bottom: A spectrum of the measured data (black, solid line) and the random coincidence background spectrum (red, dashed line) for an incident neutron energy of $E_n^{inc} = 2.0-3.0$ MeV, which corresponds to an average incident energy of $\langle E_n^{inc} \rangle = 2.514$ MeV. See the text for a discussion of both figures.

uncertainty sum in quadrature to less than 1% for the majority of the reported PFNS neutron energy range, which is a reflection of the fact that the contribution to background from neutron scattering is smaller for higher neutron energies (above 1–2 MeV). The liquid scintillator background was impacted by the same effects that influenced the Li-glass background measurement, but to a much lesser extent as a smaller percentage of the measured data resulted from random backgrounds. This background has the same form as in Eq. (19), but with $\sigma_{b,r}$, the systematic uncertainty from random rate changes during the course of an experiment calculated from Eq. (6), equal to 0.133%, and $\sigma_{b,l}$, the systematic uncertainty associated with the assumption that any three micropulses in a macropulse vary linearly with time, set to 0 as it was found to be negligible for the data after 100 μs in a macropulse included in the analysis here. Note that $\sigma_{b,r}$, would have been much higher if careful cuts on fission rates, neutron rates, and number of micropulses in a run were not enforced.

As was stated in Sec. III B, the systematic uncertainties relating to MCNP postprocessing parameters were not negligible for liquid scintillator analysis. Specifically, the pulse-

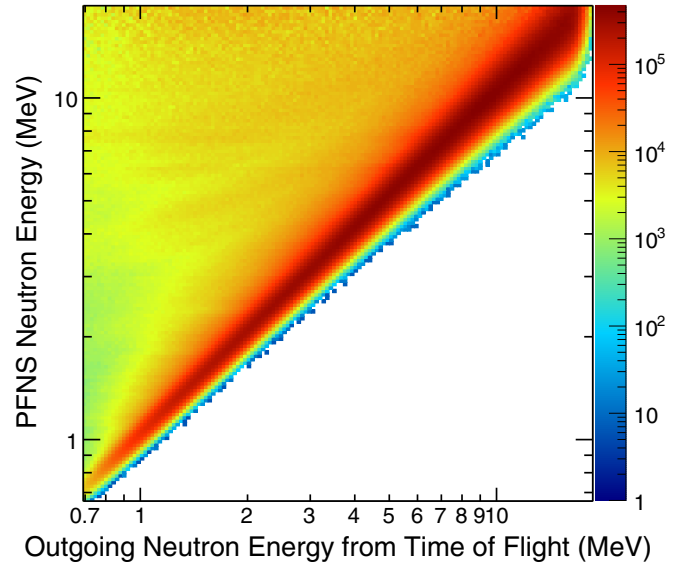


FIG. 14. The Chi-Nu liquid scintillator response matrix including a ^{239}Pu PPAC is shown here. This matrix was calculated with MCNP X-PoliMi.

height gain and pulse-height resolution parameters carried a systematic uncertainty driven by the pulse-height cutoff employed in the experimental data analysis (see the top panel of Fig. 13 or the left-hand side of Fig. 12). This pulse-height cutoff was employed to reduce the data to only those counts that are reliably described by the physics of liquid scintillator neutron detection, thereby making our PFNS results not dependent on a description of the experimental loss of counts as a function of decreasing pulse height resulting from PMT characteristics and detector thresholds in the MCNP simulation. However, this cutoff also implies that the MCNP simulation matching to the data at low pulse heights is sensitive to the accuracy of the pulse-height gain and pulse-height resolution since both of these effects can cause simulated counts to be included or excluded. This source of uncertainty is then concentrated at the lower PFNS energies of the liquid scintillator data and was part of the driver for the low-energy cutoff of approximately 850 keV outgoing neutron energy from time of flight for the liquid scintillator results shown in this work. This source of uncertainty was assumed to be the largest source of MCNP-related systematic uncertainties for the results shown here, and so uncertainties relating to nuclear physics included in the MCNP are not quantified. A detailed sensitivity study would be required for a thorough determination of the systematic uncertainties on the Li-glass and liquid scintillator PFNS results shown here, as well as the correlations between them, resulting from uncertainties in all cross sections encountered in the Chi-Nu MCNP simulation. Although an innovative framework for cross section variation within an MCNP simulation has been put forth and employed for the $^6\text{Li}(n, t)\alpha$ reaction [52], this full sensitivity study is outside the scope of this work. Covariances for the liquid scintillator MCNP parameter definitions were assessed via Monte Carlo variation of the parameters within limits constrained by the experimental data and are contained within the

covariance $\text{cov}[r]_{ij}$ in Eq. (24). These are covariances on the unnormalized liquid scintillator PFNS values themselves.

Finally, the covariance relating to the PPAC angular efficiency ($\text{cov}[\epsilon]_{ij}$) was assessed for the liquid scintillator spectra. Given the PPAC efficiency curve estimated using the method described in Sec. IID, a Monte Carlo variation of this efficiency curve was carried out using the estimated 10% uncertainty on this curve as the $1\text{-}\sigma$ for a randomly sampled Gaussian at each fragment angle. This variation yielded a covariance matrix on the liquid scintillator PFNS values that was incorporated into the total unnormalized liquid scintillator covariance matrix. This covariance corresponds to roughly a 0.4% additional uncertainty on the mean liquid scintillator PFNS energy. The total unnormalized covariance for the liquid scintillator PFNS in this work can be written as

$$\text{cov}[p]_{ij} = \frac{1}{F_i F_j} (\text{cov}[d]_{ij} + \text{cov}[b]_{ij} + p_i p_j \text{cov}[F]_{ij}) + \text{cov}[r]_{ij} + \text{cov}[\epsilon]_{ij}. \quad (24)$$

V. COMBINED PRESENTATION OF LI-GLASS AND LIQUID SCINTILLATOR PFNS RESULTS

It was shown in Ref. [26] that evaluated PFNS shapes require a normalization, and this was recently extended to experimental shape measurements in Ref. [28]. Both of these works establish the need to normalize a shape in order to obtain only the covariance relating to uncertainty in a shape. This guidance might seem to imply that both the Li-glass and liquid scintillator spectra need to be normalized separately before they can be reported, but the correct analysis requires more careful attention to details. First, the analysis methods described earlier in this work are separately applied to the Li-glass and liquid scintillator data within each incident energy bin are identical across all incident energies but separate for each detector type; the Li-glass F multiple-scattering correction factor and covariance, the relative (%) background covariance, and the relative MCNP nuclear physics covariance are identical for the Li-glass PFNS in each incident energy range, and similarly, the liquid scintillator F factor and covariance, relative background covariance, relative MCNP parameter covariance, and PPAC angular efficiency covariance are identical for each incident energy range. All of these facts create strong correlations between the PFNS results at each incident energy for each respective detector type and make clear the need to define a covariance matrix not just between PFNS points of a single detector type or between PFNS points of both detector types within an incident energy range, but between all PFNS points of both detectors *across all incident neutron energies*. Therefore, a single covariance matrix describing the entirety of the Chi-Nu results for the ^{239}Pu PFNS must be generated in order to adequately report the Chi-Nu PFNS results, as should be done with any other data set reported over multiple incident energies with similar analyses at each energy.

The constant relative covariances were used with the unnormalized PFNS centroids from each detector type to generate the covariance elements between PFNS measurements with different incident energies (i.e., the off- E_n^{inc} -diagonal

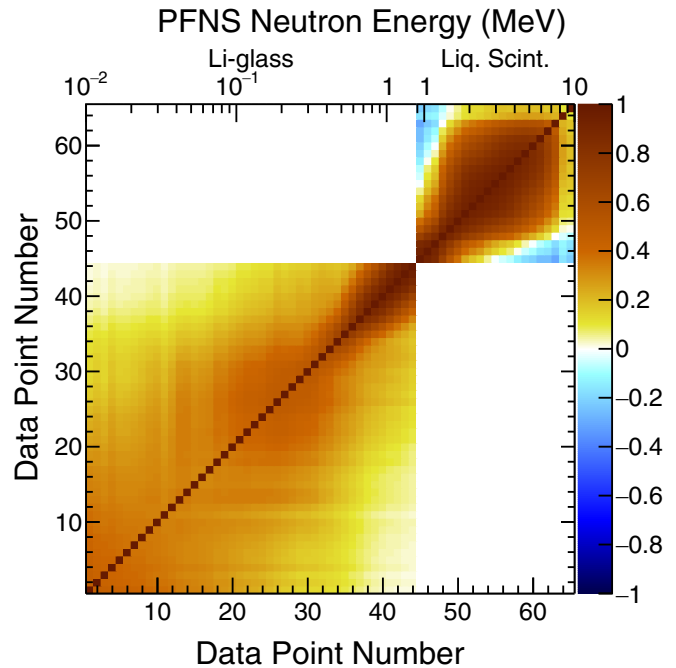


FIG. 15. The unnormalized correlation matrix associated with both the Li-glass and liquid scintillator PFNS for $E_n^{\text{inc}} = 1.0\text{--}2.0$ MeV is shown here. This matrix and those all other E_n^{inc} ranges reported in the work result directly from the covariance in Eqs. (23) and (24).

elements) of the ^{239}Pu covariance matrix. The correlation matrices associated with the Li-glass and liquid scintillator spectra for $E_n^{\text{inc}} = 1.0\text{--}2.0$ MeV are shown in Fig. 15. The same procedure is identically applied to the PFNS points corresponding to all E_n^{inc} bins, which results in a strong positive correlation between points from the same detector type but a weak correlation between points of different detector types. The data are most conveniently described in terms of data point number when considering the overlapping outgoing energies and multiple incident energy ranges. Each incident energy bin contains $N = 65$ PFNS points, $G = 44$ points from the Li-glass detectors from $E_n^{\text{out}} = 0.01\text{--}1.59$ MeV and $L = 21$ points from the liquid scintillators from $E_n^{\text{out}} = 0.89\text{--}10.0$ MeV. This yields $N_o = 5$ data points from each detector that exactly overlap with each other. All PFNS data are binned at 20 bins per decade. The PFNS neutron energies corresponding to the data point numbers within a single E_n^{inc} range are shown in the top x axis in Fig. 15. We are reporting data for 20 incident energy bins from $E_n^{\text{inc}} = 1\text{--}20$ MeV, yielding 1300 PFNS data points.

Noteworthy in Fig. 15 is that initially there are only weak correlations between the uncertainties of data points of a Li-glass and liquid scintillator data set based on wraparound corrections (see Sec. IIF), though these cross-detector correlations are difficult to see. In principle, there are additional correlations between the uncertainties of these unnormalized data sets due to, for example, being measured in the same experimental area and using the same PPAC to measure the PFNS. However, the quantification of these correlations is not

straightforward and many of these correlations will likely result from the sensitivity study mentioned in Sec. IV B, which is outside of the scope of this paper. Therefore, the existence of any additional correlations between the unnormalized Li-glass and liquid scintillator data sets will be ignored for this work.

Following the guidance of Ref. [28], we combine the Li-glass and liquid scintillator data in each incident energy range by performing a simultaneous normalization of the data from both detectors assuming that the area in the overlap region is the same. The assumption that the PFNS shapes from both detectors have the same area in the overlap region is motivated by the fact that the two detector arrays are attempting to measure the same underlying PFNS in the overlap region. However, in order to generate the normalized off- E_n^{inc} -diagonal elements of the covariance matrix across all incident energies, the methods of Ref. [28] must be extended to perform a normalization of the combined Li-glass-liquid scintillator PFNS shape of all incident energies in a single calculation. In other words, we must evaluate

$$\text{cov}[n]_{\alpha i \beta j} = \Delta_{\alpha i \lambda k} \text{cov}[p]_{\lambda k \mu l} \Delta_{\beta j \mu l}. \quad (25)$$

We are using the Einstein summation notation here, summing over the repeated λ , k , μ , and l indices. Greek indices (α , β , λ , μ) represent incident energy bins, Roman indices (i , j , k , l) represent outgoing energy bins, $n_{\alpha i}$ is the normalized PFNS for incident energy bin α and outgoing energy bin i , and

$$\Delta_{\alpha i \lambda k} = \frac{\partial n_{\alpha i}}{\partial p_{\lambda k}}. \quad (26)$$

As is described in detail in Ref. [28], the exact definition of $n_{\alpha i}$ depends on the choice of whether the unnormalized Li-glass PFNS data are scaled to have the same area as the liquid scintillators in the overlap region, or vice versa. However, in either case, the resulting PFNS centroids and covariances are identical, so we will choose to scale the liquid scintillators to have the same area as the Li-glass detectors in the overlap region such that [28]

$$n_{\alpha i} = \begin{cases} p_{\alpha i}/A_T & \text{if } 0 \leq i < G \\ \rho_{\alpha} p_{\alpha i}/A_T & \text{if } G \leq i < N \end{cases} = \frac{\rho_{\alpha}^{\theta(i)} p_i}{A_T}. \quad (27)$$

Here A_T is the total area of the combined unnormalized PFNS defined as

$$A_T = \sum_{i=0}^{G+N_o-1} p_{\alpha i} w_i + \frac{1}{2} \sum_{j=G-N_o}^{G-1} p_{\alpha j} w_j + \frac{1}{2} \sum_{k=G}^{G+N_o-1} \rho_{\alpha} p_{\alpha k} w_k + \sum_{l=G+N_o}^{L-1} \rho_{\alpha} p_{\alpha l} w_l, \quad (28)$$

and ρ_{α} is the scaling factor forcing the unnormalized liquid scintillator PFNS spectrum for E_n^{inc} range α to the same as that of the unnormalized Li-glass spectrum for the same E_n^{inc}

defined as

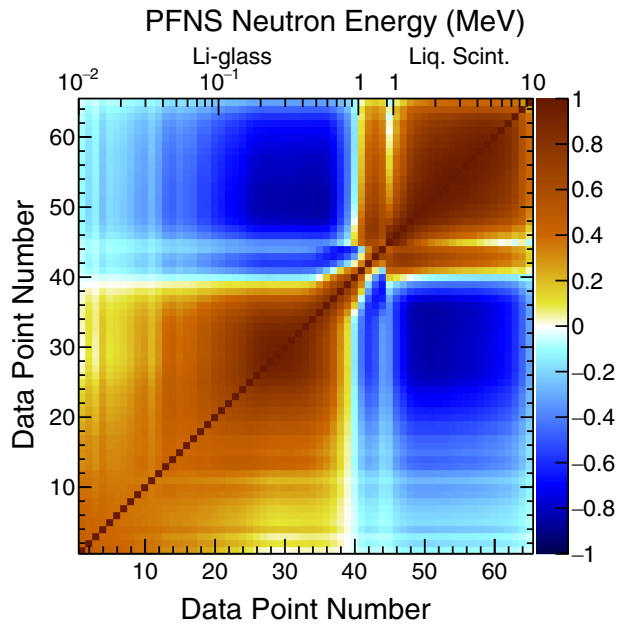
$$\rho_{\alpha} = \left[\sum_{i=G}^{G+N_o-1} p_{\alpha i} w_i \right] \times \left[\sum_{j=G-N_o}^{G-1} p_{\alpha j} w_j \right]^{-1} \quad (29)$$

where w_i is the width of PFNS bin i . The $\theta(i)$ parameter in Eq. (27) is a step function equal to 0 if i is part of a Li-glass data set, yielding $\rho_{\alpha}^0 = 1$ in Eq. (27), and equal to unity if i is part of a liquid scintillator data set, yielding $\rho_{\alpha}^1 = \rho_{\alpha}$ in Eq. (27). In this way only data points in the liquid scintillator data sets have ρ_{α} applied. The derivatives in Eq. (26) are straightforward to derive (albeit long) and are not written explicitly here.

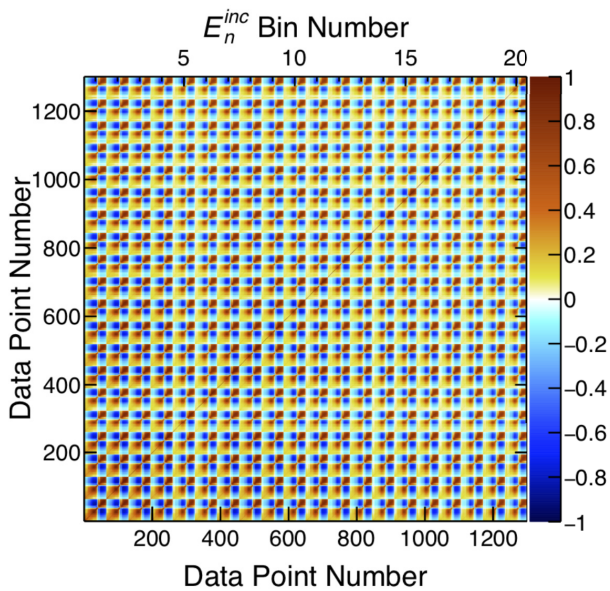
The resulting correlation matrix for the combined Li-glass-liquid scintillator PFNS within $E_n^{\text{inc}} = 1.0\text{--}2.0$ MeV is shown in Fig. 16(a) and the correlation matrix containing off- E_n^{inc} -diagonal elements is shown in Fig. 16(b), with either the individual Li-glass and liquid scintillator PFNS energies or the incident neutron energy bin divisions along the top x axis, respectively. Additionally, since a very similar analysis is used to extract the PFNS at each incident energy range, the relative systematic uncertainties are very similar for each PFNS reported here. Thus, the relative uncertainties shown graphically in Fig. 17 can be roughly interpreted as the relative uncertainties for each PFNS shown in the following sections, though the normalization procedure redistributes uncertainties in a slightly different way at each incident energy depending on the shape of the deduced PFNS.

The matrix in Fig. 16(b) fully describes the correlation between all PFNS shape data points for both detectors and all incident neutron energy bins reported in this work. The incident energy bin numbers shown along the top x axis in Fig. 16(b) correspond to an E_n^{inc} range shown in Secs. VIA–VIC. Each E_n^{inc} bin is 1 MeV wide going from 1 to 20 MeV, with bins 5 and 6 corresponding to 5.0–5.5 and 5.5–6.0 MeV respectively, to provide increased E_n^{inc} granularity for the onset of second-chance fission. This correlation across incident neutron energy bin has never been reported in a PFNS measurement publication, including other white source measurements and PFNS measurements at multiple incident energy by the same group [17,20,43], though PFNS evaluators sometimes estimate these correlations.

There are many added benefits of reporting the PFNS correlations across all measured outgoing and incident energy ranges. First, given the clearly defined correlations between all measured outgoing energies for each incident energy, the relative scaling of both the Li-glass and liquid scintillator data are constrained when included in evaluations. In the absence of these correlations, it may be possible for these data sets to scale independently of each other within a PFNS evaluation, which in turn can lead to incorrect results of a nuclear data evaluation. Additionally, the added effort required by evaluators to estimate the correlations between different PFNS measurements is eliminated. Next, the correlations across incident neutron energy allow for the generation of a covariance matrix for the mean PFNS energy as a function of incident neutron energy. While the ability to calculate this matrix is itself interesting in that no experimental $\langle E \rangle$ versus



(a)



(b)

FIG. 16. The correlation matrices shown here result from the individual normalization of the combined Li-glass-liquid scintillator PFNS at each incident energy following the procedure described in Ref. [28] and extending it to multiple incident energies. See the text for a discussion and description of the E_n^{inc} bins. The normalized correlation matrix associated with both the Li-glass and liquid scintillator PFNS for $E_n^{\text{inc}} = 1.0\text{--}2.0$ MeV is shown in panel (a), and the combined normalized correlation matrix for the Li-glass and liquid scintillator data across all incident neutron energies is shown in panel (b).

E_n^{inc} covariance matrix has ever been reported, this also allows for firm statements on the *shape* of the $\langle E \rangle$ versus E_n^{inc} trend to be made in addition to the absolute reported values, which becomes useful in Sec. VID. Finally, in principle, one could

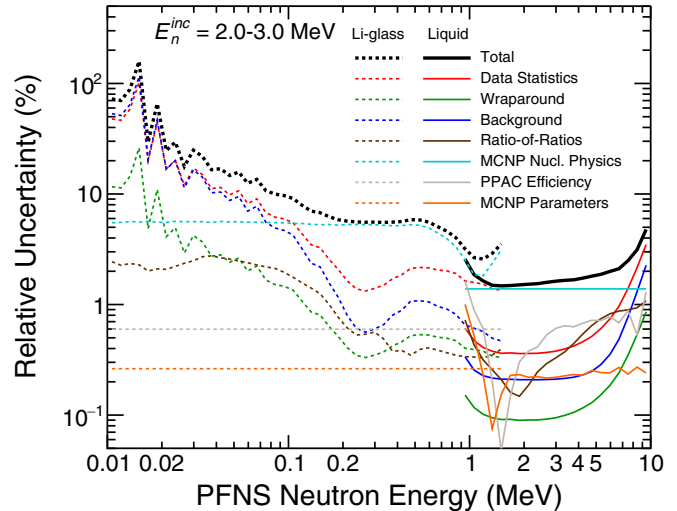


FIG. 17. Shown here are a set of representative relative uncertainties from each uncertainty source incorporated into the PFNS results shown in this work. Solid and dashed lines of the various colors correspond to liquid scintillator and Li-glass uncertainties, respectively.

study the behavior of a single or a subset of the reported PFNS energy bins as a function of incident neutron energy. While such a study has not been carried out for the present work, this example implies that there is much more depth of analysis available for the PFNS data and covariances reported here.

VI. RESULTS AND DISCUSSION

The ^{239}Pu PFNS changes as a function of the incident neutron energy inducing fission as a result of increased energy input to the $^{239}\text{Pu} + n$ system and the opening of different reaction channels. The fission reaction channels important for this work are described schematically in Fig. 18. The various paths to fission are described at the beginning of the relevant following sections. Measurements of first-chance fission only are described in Sec. VIA, measurements above the threshold for second-chance fission but below that of third-chance fission are described in Sec. VIB, and measurements above the thresholds for second- and third-chance fission and pre-equilibrium neutron emission are shown in Sec. VIC. All PFNS results in this work are shown relative to a 1.424-MeV Maxwellian distribution to eliminate the majority of the E_n^{out} dependence of the PFNS and show more clearly the non-Maxwellian PFNS features. Additionally, while we are reporting PFNS results down to 10 keV in the covariances reported in the previous section and in the mean PFNS energies reported in Sec. VID, the PFNS results plots in the following sections stop at 100 keV. We chose to report the data this way because (a) the PFNS below 100 keV comprises $\leq 3\%$ of the total integral of a PFNS and is therefore not as important as the data above 100 keV for comparison to evaluations and literature data, and (b) the data at these low energies were primarily important for validating the background treatment at the higher energies.

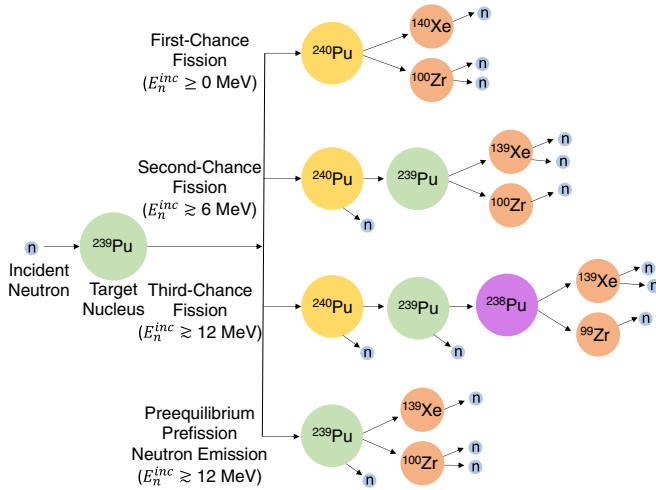


FIG. 18. Shown here are the various paths that can lead to fission for the $^{239}\text{Pu} + n$ system with the approximate incident neutron energy ranges for which they occur. Note that the chosen fission fragments are only one of the many possible combinations of fission fragment pairs. This figure is a reproduction of Fig. 1 from Ref. [53]. The various processes involving prefission neutron emission allow different nuclei to undergo fission and can create unique features in the measured spectra. Numbers of neutrons and fission fragment identities are approximate.

A. Low incident energies

For incident energies $E_n^{\text{inc}} \leq 5$ MeV, fission is believed to proceed via capture of a neutron by ^{239}Pu followed by fission of a ^{240}Pu nucleus, termed “first-chance fission.” Comparisons of the present results with existing literature data from Lestone and Shores [16] and Chatillon *et al.* [20] as well as to the ENDF/B-VIII.0 [15] and JEFF-3.3 [76] evaluations are shown in Figs. 19(a)–19(d). As was stated in the introduction of this work, the data of Chatillon *et al.* [20] were corrected for issues with the assumed efficiency curve after publication by Granier [21], which led to different centroid values than those originally reported and also to increased systematic uncertainties for the data used in ENDF/B evaluations. The corrected data with increased systematic uncertainties are shown in this work. The results of Lestone and Shores [16] were collected from neutron experiment (NUEX) diagnostics from nuclear device tests at the Nevada Test Site (NTS). As such, these results were collected with a very different method than that used here, which resulted in high statistical precision.

The ENDF/B ^{239}Pu PFNS evaluations have been driven strongly by Lestone and Shores PFNS data due to the high statistical precision, so the comparison of results at an average incident neutron energy of $\langle E_n^{\text{inc}} \rangle \approx 1.5$ MeV is an important benchmark. The upturn of the ^{239}Pu PFNS at high outgoing neutron energies suggested by Lestone and Shores is not apparent in the present results, though future extensions to $E_n^{\text{out}} \geq 10$ MeV may shed light on this potential feature. An additional detail worth noting is that six of the eight uncertainty sources listed by Lestone [77] are believed to be correlated across outgoing neutron energies, three of which are strongly correlated. These correlations combined with the

relative contribution of the correlated uncertainties imply that the shape of these data is fairly well constrained, but the uncertainty on the shape cannot be quantified because no correlation matrix has been explicitly published for these data.

B. Second-chance fission PFNS features

Beginning at $E_n^{\text{inc}} \approx 5.0$ – 6.0 MeV it is possible for the ^{240}Pu compound nucleus to emit a neutron prior to the fission event, leading to fission of a ^{239}Pu nucleus. The emission of this neutron and the change in identity of the fissioning nucleus introduces unique features into the observed PFNS. As mentioned in the Introduction, the neutron emitted prior to fission is not strictly a prompt fission neutron, i.e., a neutron emitted promptly following fission. However, the short timescales involved in nuclear fission make it experimentally impossible to separate these prefission neutrons from postfission PFNS neutrons, and so both pre- and postfission neutrons appear in the experimental spectrum.

The PFNS results from the Chi-Nu experiment from $E_n^{\text{inc}} = 5.0$ – 10.0 MeV are shown in Figs. 20(a)–20(f) with comparisons to the same literature and evaluated spectra as shown in Sec. VI A. The emergence of second-chance fission can be seen in the $E_n^{\text{inc}} = 6.0$ MeV ENDF/B-VIII.0 evaluation in Figs. 20(a) and 20(b) as the increased relative PFNS value from $E_n^{\text{out}} = 100$ – 500 keV. The existence of the feature in the present results becomes clear in Fig. 20(b). The data of Chatillon *et al.* provide little insight into this PFNS feature because of the higher threshold of those measurements. Both the JEFF-3.3 and ENDF/B-VIII.0 evaluations appear to generally agree within uncertainties with the present results, though shape differences are apparent between the evaluations, especially above $E_n^{\text{out}} \approx 4$ – 5 MeV.

C. Pre-equilibrium neutron component and third-chance fission

Above $E_n^{\text{inc}} \approx 12$ MeV two new fission paths are expected to become available: third-chance fission and pre-equilibrium neutron emission preceding fission. Third-chance fission is conceptually similar to second-chance fission in that a prefission neutron is emitted from a compound nucleus, whereas in second-chance fission a prefission neutron is emitted from ^{240}Pu leading to fission of a ^{239}Pu , in third-chance fission a second prefission neutron is emitted from ^{239}Pu leading to fission of a ^{238}Pu nucleus. Pre-equilibrium neutron emission preceding fission is also similar to second-chance fission in that a ^{239}Pu nucleus undergoes fission. However, as opposed to the emission of neutron from a ^{240}Pu compound nucleus in second-chance fission, there is no compound ^{240}Pu nucleus formed in the pre-equilibrium process. Instead, an incident neutron effectively undergoes an inelastic scattering reaction leaving the residual ^{239}Pu with enough excitation energy to fission. The pre-equilibrium reaction process is also known to result in a distinct, forward-peaked angular distribution for the prefission neutron as was recently shown in Ref. [53].

Figures 21(a)–21(e) and 22(a)–22(e) show the present results for $E_n^{\text{inc}} = 10.0$ – 15.0 MeV and 15.0 – 20.0 MeV, respectively. The third-chance fission features predicted in the evaluated PFNS can be seen in the ENDF/B-VIII.0 and

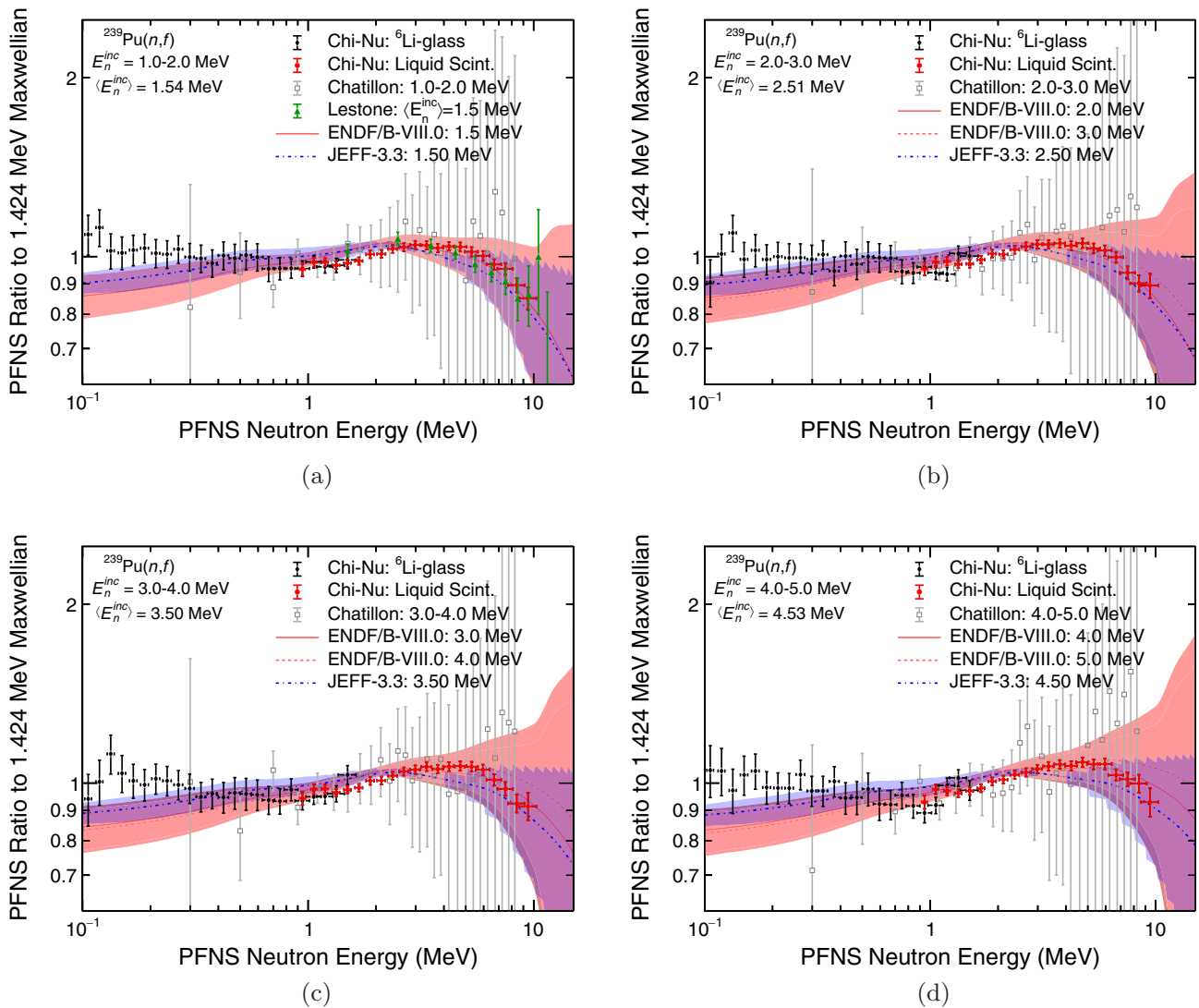


FIG. 19. Shown here are comparisons of the present PFNS results with the spectra from Lestone and Shores [16] and Chatillon *et al.* [20] as well as the ENDF/B-VIII.0 [15] and JEFF-3.3 [76] evaluations at the relevant incident neutron energies. The band for each evaluation trend represents the $1\text{-}\sigma$ uncertainty limit. Note that the evaluation spectra are evaluated at a single E_n^{inc} value and the other experiment spectra are integrated over different E_n^{inc} ranges. See the text for a discussion. (a) The PFNS for $E_n^{\text{inc}} = 1.0\text{--}2.0$ MeV, corresponding to an average incident neutron energy $\langle E_n^{\text{inc}} \rangle = 1.54$ MeV, (b) The PFNS for $E_n^{\text{inc}} = 2.0\text{--}3.0$ MeV, corresponding to an average incident neutron energy $\langle E_n^{\text{inc}} \rangle = 2.51$ MeV, (c) The PFNS for $E_n^{\text{inc}} = 3.0\text{--}4.0$ MeV, corresponding to an average incident neutron energy $\langle E_n^{\text{inc}} \rangle = 3.50$ MeV, and (d) The PFNS for $E_n^{\text{inc}} = 4.0\text{--}5.0$ MeV, corresponding to an average incident neutron energy $\langle E_n^{\text{inc}} \rangle = 4.53$ MeV.

JEFF-3.3 curves on these plots as the increase in relative PFNS contribution at $E_n^{\text{out}} \approx 100\text{--}500$ keV beginning in Fig. 21(c) and moving up through the spectrum in the higher E_n^{inc} plots. Interestingly, there appears to be minimal evidence for this feature in the present experimental results. The difference in the measured and evaluated PFNS contributions from third-chance fission becomes more obvious when the mean PFNS energy is considered in Sec. VID.

The pre-equilibrium component of the PFNS can be seen starting in Fig. 21(a) as the peak at $E_n^{\text{out}} \approx 5$ MeV. This peak moves toward increasing E_n^{out} and becomes more sharply peaked as E_n^{inc} increases through Figs. 21(a)–22(d). In general, the position and magnitude of this feature in the PFNS agrees well with the ENDF/B-VIII.0 and JEFF-3.3 evaluations. The clarity with which this PFNS feature is observed in the

present results allowed for the relative contribution of the pre-equilibrium peak to the PFNS to be extracted from the data as a function of liquid scintillator detection angle from $E_n^{\text{inc}} = 14\text{--}20$ MeV. The results of this analysis are described in Ref. [53]. Since only the minimally necessary details of the analysis were provided in Ref. [53], we will elaborate on the procedure for extracting the angular distribution of the pre-equilibrium peak counts in the remainder of this section.

In order to extract the angular distribution of the pre-equilibrium peak in the observed PFNS spectrum, the counts in this peak (not the relative PFNS contribution) need to be calculated by extracting these counts much like a peak above background. This approach implies that a description of the “background” spectrum underlying the pre-equilibrium peak at each considered E_n^{inc} and angle is required. Although

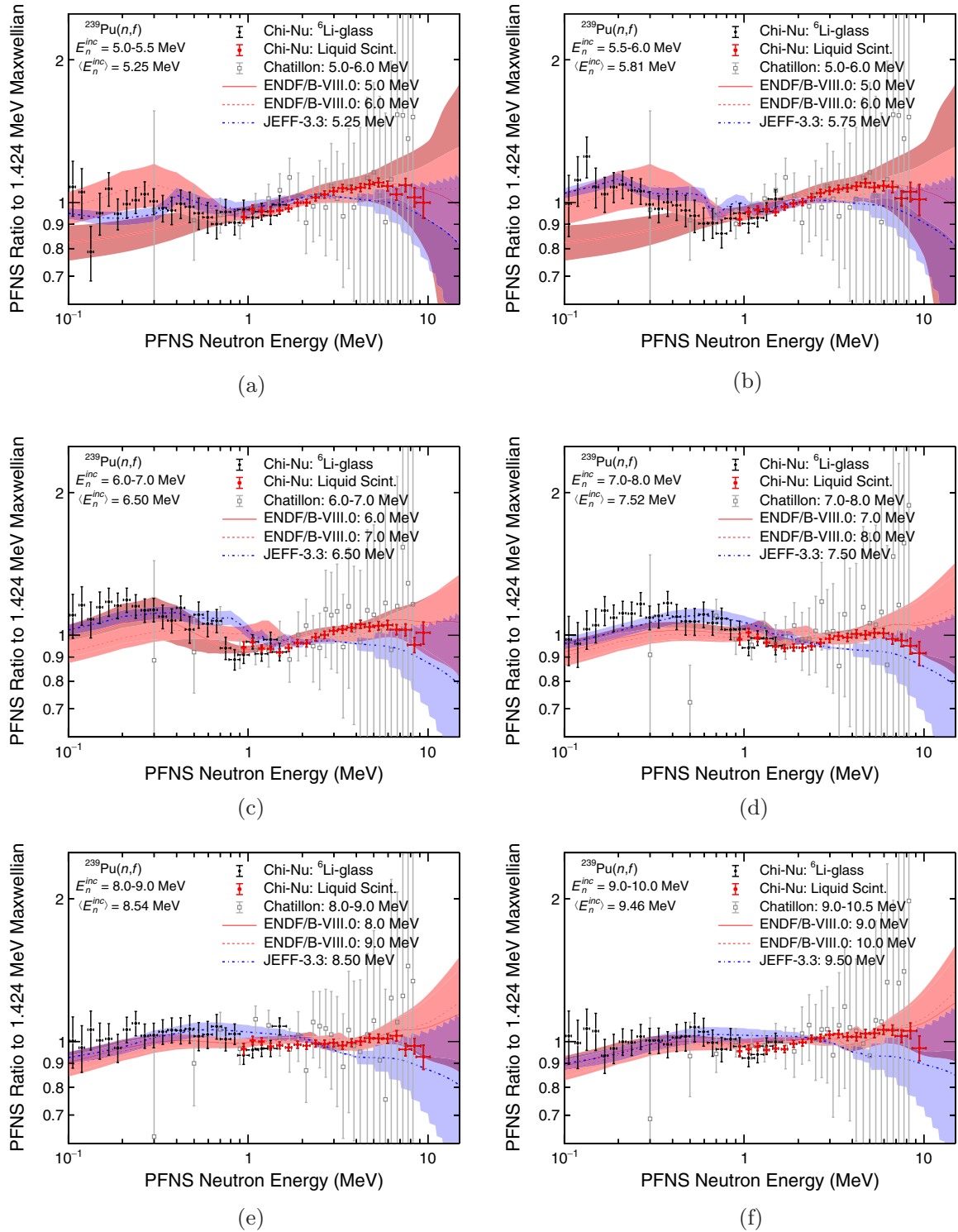


FIG. 20. Shown here are comparisons of the present PFNS results with the spectra from Chatillon *et al.* [20] and the ENDF/B-VIII.0 [15] and JEFF-3.3 [76] evaluations for E_n^{inc} ranges corresponding to a combination of first- and second-chance fission. The band for each evaluation trend represents the $1\text{-}\sigma$ uncertainty limit. Note that the evaluation spectra are evaluated at a single E_n^{inc} value and the other experiment spectra are integrated over different E_n^{inc} ranges. See the text for a discussion. (a) The PFNS for $E_n^{\text{inc}} = 5.0\text{--}5.5$ MeV, corresponding to an average incident neutron energy $E_n^{\text{inc}} = 5.25$ MeV, (b) The PFNS for $E_n^{\text{inc}} = 5.5\text{--}6.0$ MeV, corresponding to an average incident neutron energy $E_n^{\text{inc}} = 5.81$ MeV, (c) The PFNS for $E_n^{\text{inc}} = 6.0\text{--}7.0$ MeV, corresponding to an average incident neutron energy $E_n^{\text{inc}} = 6.50$ MeV, (d) The PFNS for $E_n^{\text{inc}} = 7.0\text{--}8.0$ MeV, corresponding to an average incident neutron energy $E_n^{\text{inc}} = 7.52$ MeV, (e) The PFNS for $E_n^{\text{inc}} = 8.0\text{--}9.0$ MeV, corresponding to an average incident neutron energy $E_n^{\text{inc}} = 8.54$ MeV, and (f) The PFNS for $E_n^{\text{inc}} = 9.0\text{--}10.0$ MeV, corresponding to an average incident neutron energy $E_n^{\text{inc}} = 9.46$ MeV.

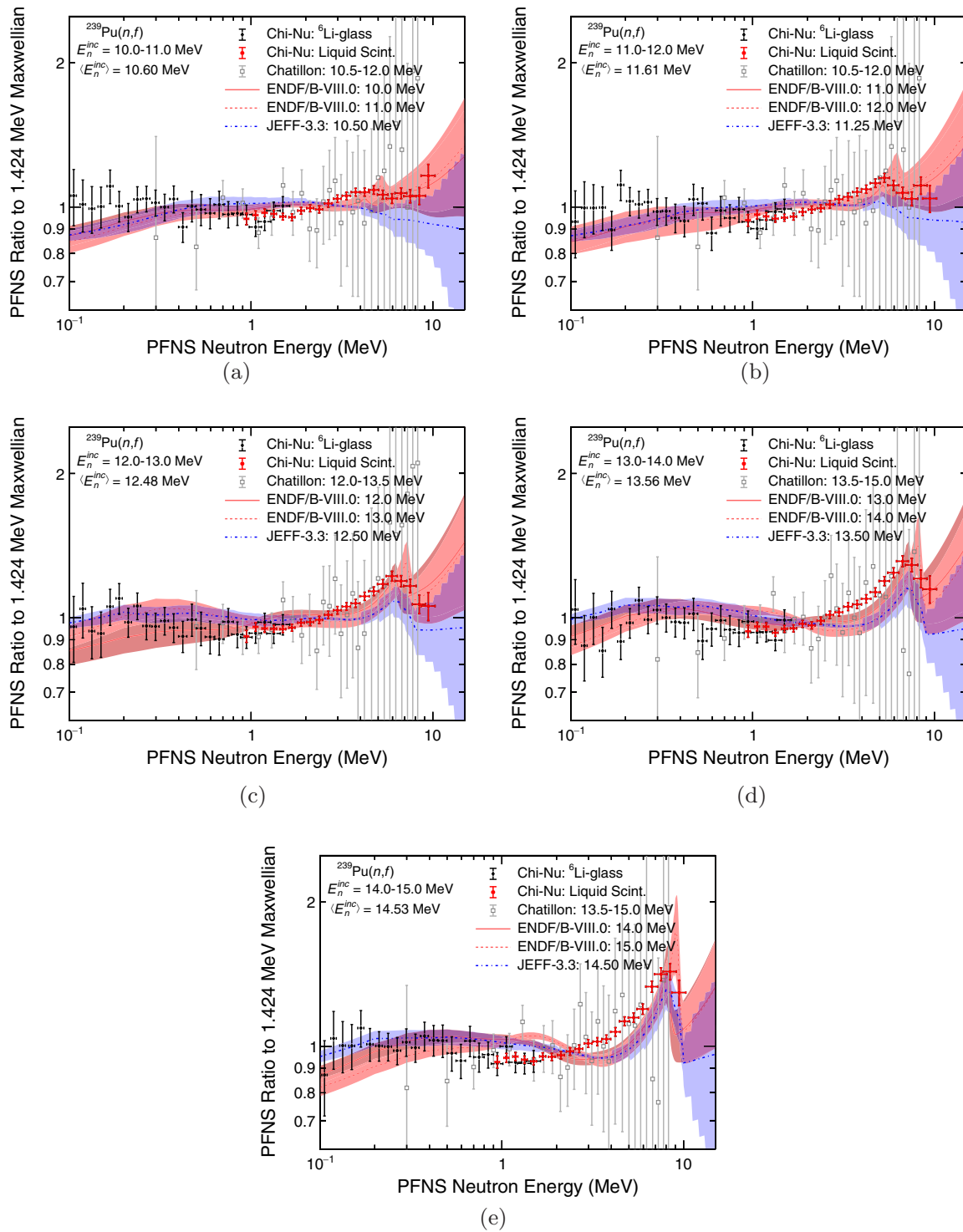


FIG. 21. Shown here are comparisons of the present PFNS results with the spectra from Chatillon *et al.* [20] and from the ENDF/B-VIII.0 [15] and JEFF-3.3 [76] evaluations for E_n^{inc} ranges corresponding to a combination of first-, second-, and third-chance fission as well as pre-equilibrium neutron emission preceding fission from $E_n^{\text{inc}} = 10\text{--}15$ MeV. The band for each evaluation trend represents the $1\text{-}\sigma$ uncertainty limit. Note that the evaluation spectra are evaluated at a single E_n^{inc} value and the other experiment spectra are integrated over different E_n^{inc} ranges. See the text for a discussion. (a) The PFNS for $E_n^{\text{inc}} = 10.0\text{--}11.0$ MeV, corresponding to an average incident neutron energy $\langle E_n^{\text{inc}} \rangle = 10.60$ MeV, (b) The PFNS for $E_n^{\text{inc}} = 11.0\text{--}12.0$ MeV, corresponding to an average incident neutron energy $\langle E_n^{\text{inc}} \rangle = 11.61$ MeV, (c) The PFNS for $E_n^{\text{inc}} = 12.0\text{--}13.0$ MeV, corresponding to an average incident neutron energy $\langle E_n^{\text{inc}} \rangle = 12.48$ MeV, (d) The PFNS for $E_n^{\text{inc}} = 13.0\text{--}14.0$ MeV, corresponding to an average incident neutron energy $\langle E_n^{\text{inc}} \rangle = 13.56$ MeV, and (e) The PFNS for $E_n^{\text{inc}} = 14.0\text{--}15.0$ MeV, corresponding to an average incident neutron energy $\langle E_n^{\text{inc}} \rangle = 14.53$ MeV.

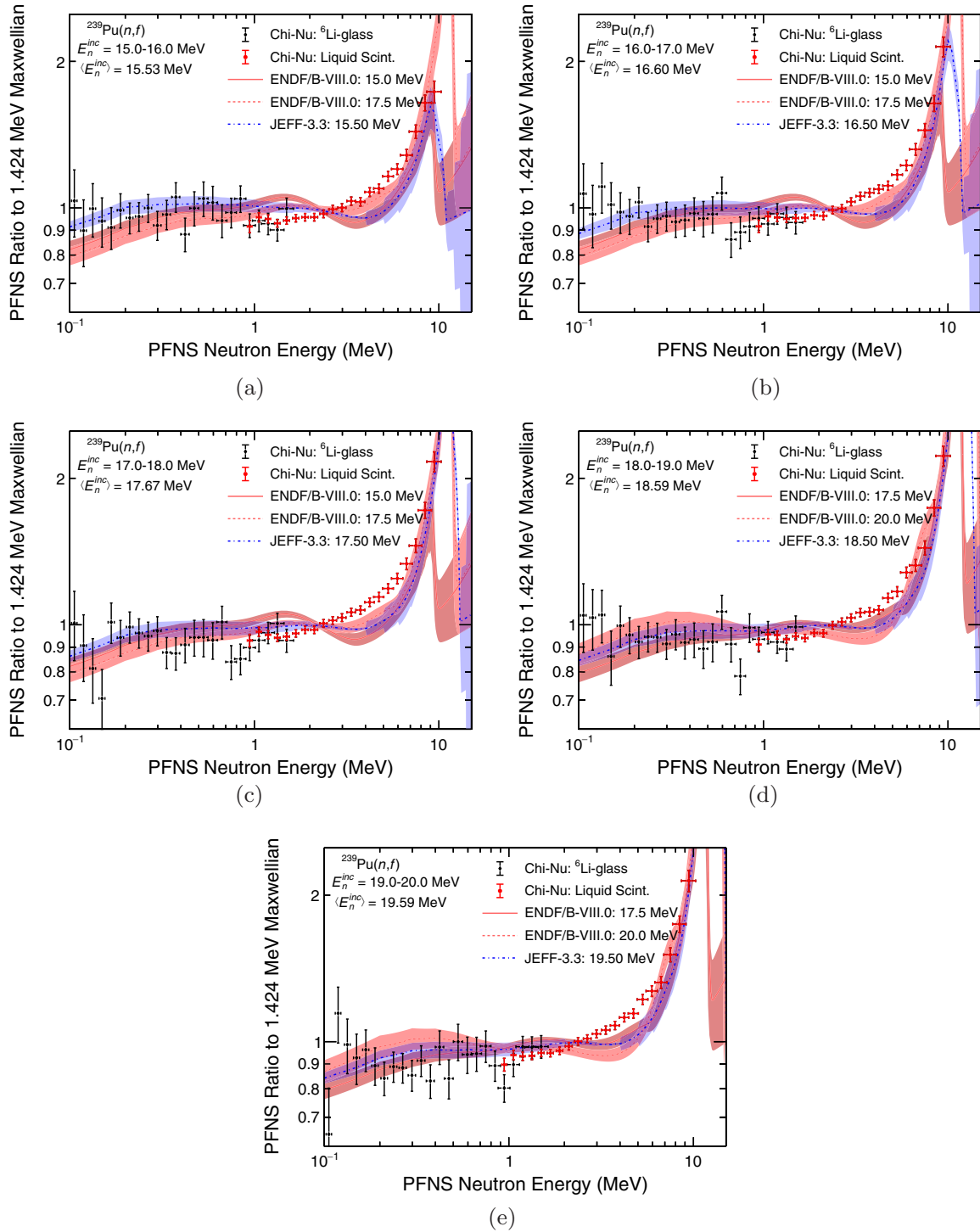


FIG. 22. Shown here are comparisons of the present PFNS results with the ENDF/B-VIII.0 [15] and JEFF-3.3 [76] evaluations for E_n^{inc} ranges corresponding to a combination of first-, second-, and third-chance fission as well as pre-equilibrium neutron emission preceding fission from $E_n^{inc} = 15\text{--}20.0$ MeV. The band for each evaluation trend represents the $1\text{-}\sigma$ uncertainty limit. The data of Chatillon *et al.* were excluded from the ENDF/B-VIII.0 ^{239}Pu PFNS evaluation for these incident energies, so they are not shown here. Note that the evaluation spectra are evaluated at a single E_n^{inc} value and the other experiment spectra are integrated over different E_n^{inc} ranges. See the text for a discussion. (a) The PFNS for $E_n^{inc} = 15.0\text{--}16.0$ MeV, corresponding to an average incident neutron energy $\langle E_n^{inc} \rangle = 15.53$ MeV, (b) The PFNS for $E_n^{inc} = 16.0\text{--}17.0$ MeV, corresponding to an average incident neutron energy $\langle E_n^{inc} \rangle = 16.60$ MeV, (c) The PFNS for $E_n^{inc} = 17.0\text{--}18.0$ MeV, corresponding to an average incident neutron energy $\langle E_n^{inc} \rangle = 17.67$ MeV, (d) The PFNS for $E_n^{inc} = 18.0\text{--}19.0$ MeV, corresponding to an average incident neutron energy $\langle E_n^{inc} \rangle = 18.59$ MeV, and (e) The PFNS for $E_n^{inc} = 19.0\text{--}20.0$ MeV, corresponding to an average incident neutron energy $\langle E_n^{inc} \rangle = 19.56$ MeV.

the pre-equilibrium component of the PFNS is a distribution that is more broad than just the peak itself, the spectrum underlying the pre-equilibrium peak can be approximated as being dominated by the postfission PFNS spectrum [78]. However, while simple PFNS models such as Maxwellian or Watt distributions may be able to describe a given PFNS shape, especially within a restricted E_n^{out} range, no simple model exists to describe the shape of the measured counts because of complicated interactions of neutrons with the experimental environment. Therefore, the measured spectrum must be converted to a PFNS in order to obtain a description of the counts underlying the pre-equilibrium peak using a Watt function. This Watt function must then be converted back to counts to allow for a subtraction of background in counts from the pre-equilibrium peak region of the measured spectrum. Finally, these counts, measured as a function of E_n^{inc} and neutron detection angle, describe the shape of the pre-equilibrium peak angular distribution.

To accomplish the task described above, the experimental spectrum was converted to a fission neutron spectrum using a ratio to ^{252}Cf . The ^{252}Cf data were collected just prior to collection of the ^{239}Pu data shown in this work using a ^{252}Cf PPAC that is nearly identical to the ^{239}Pu PPAC. Mathematically, this conversion was accomplished via

$$p_{\text{Pu}}(E, \theta) = \frac{c_{\text{Pu}}(E, \theta)}{c_{\text{Cf}}(E, \theta)} p_{\text{Cf}}(E), \quad (30)$$

where θ is the laboratory detection angle; $c(E)$ and $p(E)$ are experimental counts and the PFNS, respectively; and the subscripts *Pu* and *Cf* refer to $^{239}\text{Pu}(n, f)$ and $^{252}\text{Cf}(\text{sf})$ spectra. In principle, the energies in Eq. (30) are neutron time-of-flight energies, but the PFNS is defined in terms of the initial neutron energy, E (the PFNS neutron energy). As mentioned in Sec. II C, the method of measuring a PFNS as a ratio to ^{252}Cf does not generally produce accurate results because this method incorrectly assumes that the environmental neutron scattering correction to the data of interest, ^{239}Pu in this case, is identical to that of $^{252}\text{Cf}(\text{sf})$ [66,67]. However, the purpose of this calculation is *not* to report a PFNS for ^{239}Pu as a ratio to $^{252}\text{Cf}(\text{sf})$, and in fact the calculation of the PFNS via Eq. (30) is reversed after the PFNS underlying the pre-equilibrium region has been characterized, as described in the previous paragraph. This makes the method of PFNS calculation somewhat arbitrary for the analysis here with the only requirement being that the measured counts are transformed into a spectrum amenable to description via a simple PFNS model, which the ratio-to- ^{252}Cf calculation in Eq. (30) satisfies.

Covariances from the ^{239}Pu and ^{252}Cf counts as well as from the ENDF/B-VIII.0 [15] $^{252}\text{Cf}(\text{sf})$ PFNS used for this analysis were propagated through to the calculated PFNS. Next, a Watt function was fit to the PFNS spectrum *excluding* the pre-equilibrium peak region for the spectrum at each energy and angle, keeping this region constant across spectra at each angle even if the pre-equilibrium component cannot be seen at a given angle. The Watt spectrum is

given by [2,3]

$$\chi_w(E; a, b, N) = \frac{2N}{\sqrt{\pi a^3 b}} \sinh(\sqrt{bE}) \times \exp\left[-\frac{ab}{4} - \frac{E}{a}\right], \quad (31)$$

where

$$a = T \quad \text{and} \quad b = \frac{4E_f}{T^2}. \quad (32)$$

The parameters T and E_f are the nuclear temperature at the time of neutron emission and the kinetic energy of the fission fragment in the laboratory frame prior to neutron emission. For the fit, a normalization parameter, N , was included as well to allow the Watt function to be on the same scale as the data. The Watt function can be described in parameter space, yielding the function $\chi_w(E; a, b, N)$ which must be evaluated at each incident energy, E , to obtain a value of the Watt spectrum, or it can be described as a pointwise function of energy, $\chi_w(E)$. While the former is the more common description of this function, the latter is advantageous for calculations described later in this section.

The fit to the PFNS *excluding* the pre-equilibrium region provides a description of the PFNS “background” underneath the pre-equilibrium counts of interest. Resulting from the fit is the covariance matrix for the Watt function in parameter space, $\text{cov}[\chi_w(E; a, b, N)]$. It can be shown that the covariance of this function in energy space is given by

$$\text{cov}[\chi_w(E)]_{ij} = \chi_w(E_i)\chi_w(E_j) \times \sum_{q=0}^{N_{\text{par}}} \sum_{r=0}^{N_{\text{par}}} \partial_{q_i} \text{cov}[\chi_w(E; a, b, N)]_{qr} \partial_{r_j}, \quad (33)$$

where q and r are indices for the Watt fit parameters, N_{par} is the number of parameters in the Watt fit, and

$$\partial_{q_i} = \frac{1}{\chi_w(E_i)} \frac{\partial}{\partial q} \chi_w(E)|_{E_i}. \quad (34)$$

Given the Watt fit function for the PFNS background underlying the pre-equilibrium peak in energy space, the Watt spectrum was then converted to counts, by *reversing* the PFNS calculation shown in Eq. (30). This yields the Watt spectrum counts

$$c_w(E, \theta) = \frac{\chi_w(E, \theta)}{p_{\text{Cf}}(E)} c_{\text{Cf}}(E, \theta). \quad (35)$$

Note that since the uncertainties from the ^{252}Cf counts and PFNS were already included prior to the fit, they were not included again at this step of the analysis. We finally obtain the counts in the pre-equilibrium peak region, $c_{pe}(E_n^{\text{inc}}, \theta)$, from

$$c_{pe}(E_n^{\text{inc}}, \theta) = \sum_{i=\text{low}}^{\text{high}} [c_{\text{Pu}}(E_i, \theta) - c_w(E_i, \theta)], \quad (36)$$

where the sum from “low” to “high” indicates the lowest and highest outgoing energy bins of the data associated with the pre-equilibrium peak region at a given incident neutron

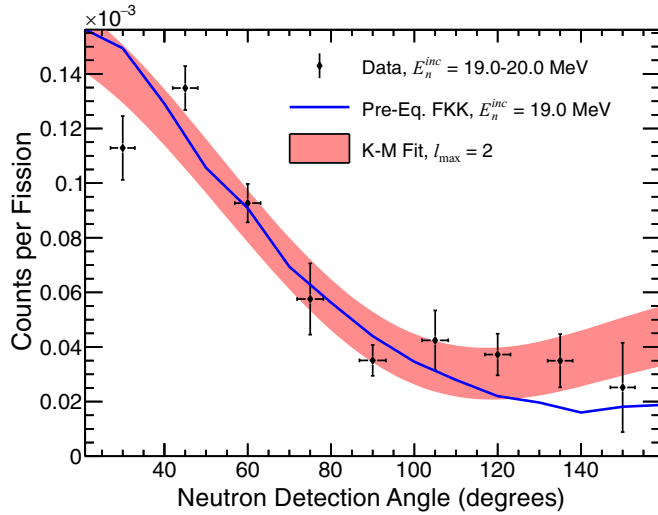


FIG. 23. Shown here is an example pre-equilibrium peak angular distribution from $^{239}\text{Pu}(n, f)$ for $E_n^{\text{inc}} = 19\text{--}20$ MeV. The measured data are shown as the black diamonds and a fit to the data using Kalbach-Mann systematics [84] and a maximum Legendre polynomial l value of 2 is shown as the red shaded region. An independent Feshbach, Kerman, and Koonin calculation for inelastically scattered neutrons from ^{239}Pu [78,79] is shown as the blue line. Note that this figure is a reproduction of Fig. 5(f) in Ref. [53]. The reader is referred to Ref. [53] for the full presentation of these results.

energy. The associated covariance matrix is described by

$$\begin{aligned} \text{cov}[c_{pe}(E_n^{\text{inc}}, \theta)]_{ij} &= \sum_{i=\text{low}}^{\text{high}} \delta_{ij} \sigma_{\text{pu},i}^2 + \sum_{i=\text{low}}^{\text{high}} \sum_{j=\text{low}}^{\text{high}} \frac{c_{\text{Cf}}(E_i) c_{\text{Cf}}(E_j)}{p_{\text{Cf}}(E_i) p_{\text{Cf}}(E_j)} \text{cov}[\chi_w(E)]_{ij}, \end{aligned} \quad (37)$$

where $\sigma_{\text{pu},i}^2$ is the covariance of the ^{239}Pu data counts (including pre-equilibrium) from counting statistics, which were not included previously because the pre-equilibrium region was excluded from the fit. The covariance of these data is diagonal, hence the Kronecker delta function, δ_{ij} . An example of an extracted pre-equilibrium peak angular distribution is shown in Fig. 23 for $E_n^{\text{inc}} = 19\text{--}20$ MeV. These distributions of pre-equilibrium peak counts were shown to agree well with the scattering model of Feshbach, Kerman, and Koonin [78,79], which provides support to the theory that these pre-equilibrium neutrons preceding fission can indeed be treated as purely scattered neutrons in coincidence with fission. Additionally, the measured angular distributions provide further information on pre-equilibrium angular distributions for fission models, especially those that use the exciton model [80–82] to describe only the energy distribution of the pre-equilibrium component of the PFNS [4–7,10,13,15,83], though some have adopted a combination of the exciton model with Kalbach-Mann systematics for this purpose [10,84]. See Ref. [53] for further discussion on this topic.

D. Mean PFNS energies

In addition to analyzing PFNS shape differences as a function of E_n^{out} and E_n^{inc} , it is informative to also calculate the mean energy of the PFNS, $\langle E \rangle$, as a function of E_n^{inc} . This amounts to a PFNS-weighted average over the E_n^{out} energies calculated as

$$\langle E \rangle_{\alpha} = \frac{\sum_i \left(\frac{1}{2}\right)^{\theta_v(i)} n_{\alpha i} w_i E_i}{\sum_j \left(\frac{1}{2}\right)^{\theta_v(j)} n_{\alpha j} w_j} = \frac{A_{w\alpha}}{A_{\alpha}}. \quad (38)$$

As in Sec. V, Greek indices indicate E_n^{inc} bins and Roman indices indicate E_n^{out} bins, $n_{\alpha i}$ is the normalized PFNS value at E_n^{out} bin i and E_n^{inc} bin α , and w_i is the width of E_n^{out} bin i , which is constant across E_n^{inc} . Here $A_{w\alpha}$ and A_{α} are the weighted and unweighted area of the PFNS at E_n^{inc} bin α , respectively. Finally, $\theta_v(i)$ is a step function equal to unity if i corresponds to data points in the overlap region between Li-glass and liquid scintillator data and is used to avoid double counting the data in the detector overlap region.

Given that the present results are described with a covariance matrix correlating all data points from both detector arrays across all measured outgoing *and* incident neutron energies, it is possible to calculate the covariance matrix of $\langle E \rangle$. This has never been done in the publication of any experimental PFNS measurement, and can provide detailed information on the experimental $\langle E \rangle$ values relative to one another (i.e., the *shape* of the $\langle E \rangle$ trend) that was previously only limited to speculation.

The $\langle E \rangle$ covariance matrix is calculated via

$$\text{cov}[\langle E \rangle]_{\alpha,\beta} = \left(\frac{\partial \langle E \rangle_{\alpha}}{\partial n_{\lambda k}} \right) \text{cov}[n]_{\lambda k \mu l} \left(\frac{\partial \langle E \rangle_{\beta}}{\partial n_{\mu l}} \right), \quad (39)$$

where $\text{cov}[n]_{\lambda k \mu l}$ is taken from Eq. (25). We have again used the Einstein summation notation to indicate summing over indices λ , k , μ , and l . The $\langle E \rangle$ derivatives can be shown to be

$$\frac{\partial \langle E \rangle_{\alpha}}{\partial n_{\lambda k}} = \left(\frac{1}{2} \right)^{\theta_v(k)} \delta_{\alpha\lambda} \frac{w_k}{A_{\alpha}} [E_k - \langle E \rangle_{\alpha}], \quad (40)$$

and so

$$\begin{aligned} \text{cov}[\langle E \rangle]_{\alpha,\beta} &= \delta_{\alpha\lambda} \delta_{\beta\mu} \left[\frac{w_k w_l}{A_{\alpha} A_{\beta}} \right] \left(\frac{1}{2} \right)^{\theta_v(k)+\theta_v(l)} \\ &\times (E_k - \langle E \rangle_{\alpha}) (E_l - \langle E \rangle_{\beta}) \text{cov}[n]_{\lambda k \mu l}, \end{aligned} \quad (41)$$

where we are implicitly summing over the same indices as in Eq. (39), and the $\delta_{\alpha\lambda}$ and $\delta_{\beta\mu}$ Kronecker δ functions require that the derivatives of $\langle E \rangle$ be within the the same E_n^{inc} bin.

The $\langle E \rangle$ results from the present work are shown in Fig. 24 with total uncertainties in black and statistical uncertainties in red compared to the ENDF/B-VIII.0 [15], JEFF-3.3 [76], and JENDL-4.0 [85] evaluations. All $\langle E \rangle$ trends are integrated from $E_n^{\text{out}} = 0.01\text{--}10$ MeV. Note that the uncertainties for the $\langle E \rangle$ results reported in this work correspond to the normalized PFNS combined across both Li-glass and liquid scintillator detector arrays. As such, the uncertainties on the present results are suitable for a shape measurement and would not be directly comparable to uncertainties from a result that, for example, considered only the statistical uncertainties with out

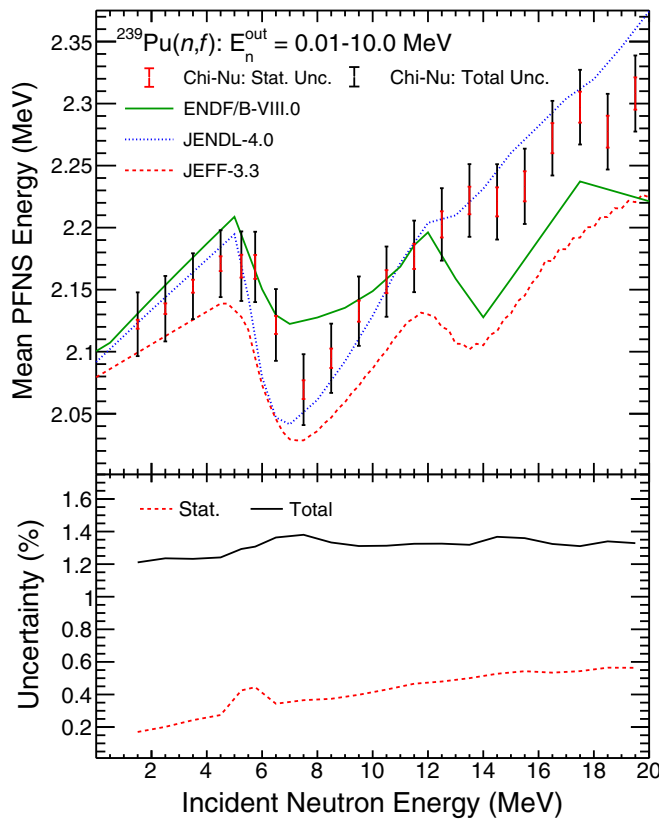


FIG. 24. Top: Shown here is the mean PFNS energy trend for the present results compared to the ENDF-B/VIII.0 [15], JEFF-3.3 [76], and JENDL-4.0 [85] evaluations shown as the red solid, blue dashed, and green dotted lines, respectively. The present results are shown as uncertainty bands only, with the net statistical uncertainty of the normalized PFNS results combined across Li-glass and liquid scintillator spectra shown as the smaller, red uncertainty band and the total uncertainty as the larger black uncertainty band. Note that each point on this plot corresponds to a PFNS distribution shown in Secs. VIA–VIC. Bottom: The percentage uncertainty trends for the statistical and total uncertainties are shown here as the solid black and red dashed lines.

a data normalization applied. The dips seen in the $\langle E \rangle$ trend at $E_n^{\text{inc}} \approx 7$ and 14 MeV in the ENDF/B-VIII.0 evaluation trend correspond to the introduction of the low E_n^{out} PFNS features that are expected to emerge in the PFNS as second- and third-chance fission channels open up. The placement of the second-chance fission feature from all three evaluations shown seems to agree well with the present results, though JEFF-3.3 and JENDL-4.0 appear to be too low in $\langle E \rangle$ at the minimum. Similar to the conclusion from the PFNS spectra shown in Sec. VIC, third-chance fission does not appear to contribute as strongly to the PFNS $\langle E \rangle$ values as predicted by the ENDF/B-VIII.0 evaluation. The JEFF-3.3 evaluation predicts a smaller contribution from third-chance fission, which is closer to the conclusion from the present results, but the overall magnitude of this evaluation appears to be too low across all E_n^{inc} values. Interestingly, JENDL-4.0 appears to agree better with the present results above 10 MeV in terms of $\langle E \rangle$ magnitude. It is difficult to make any

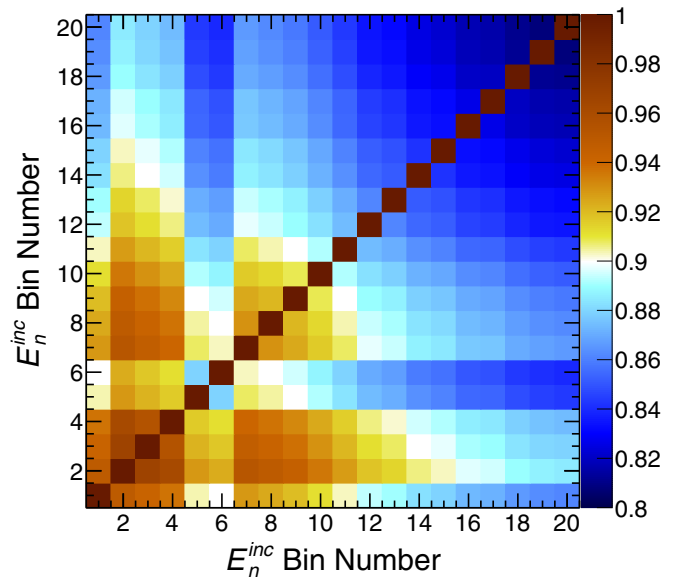


FIG. 25. Shown here is the correlation matrix between the $\langle E \rangle$ points shown in Fig. 24. Note that the z -axis scale only goes down to 0.8 , with white indicating a correlation of 0.9 , implying that all $\langle E \rangle$ points are highly correlated.

conclusions regarding the pre-equilibrium PFNS component from the $\langle E \rangle$ trend alone. The additional uncertainty sources that are intended to be added to the present results in the future are likely to carry with them reasonably strong correlations and will therefore not impact this interpretation of the $\langle E \rangle$ significantly.

The correlation matrix corresponding to the present $\langle E \rangle$ results is shown in Fig. 25. It must be noted that the z -axis scale only goes from 0.8 – 1 , and thus all $\langle E \rangle$ points are highly correlated. This conclusion was thought to be true prior to the calculation of $\langle E \rangle$ covariance matrix, but it has not been proven to be true before this work. This high level of correlation implies that the *shape* of the $\langle E \rangle$ trend is known to a much higher precision than the total uncertainties on Fig. 24 imply. The shape uncertainties themselves are not shown in Fig. 24 to avoid adding too much detail to this plot, but the shape uncertainty closely resembles the statistical uncertainty. Given that the shape is known approximately as well as the statistical uncertainties, the statistical uncertainties themselves can be interpreted as the uncertainty within which the $\langle E \rangle$ points may vary with respect to one another in a manner that impacts the shape, and the difference between the total and statistical uncertainties can be roughly interpreted to be the uncertainty that only amounts to a constant scaling of the $\langle E \rangle$ trend. Therefore, the present results are consistent with a weak onset of third-chance fission.

Finally, concerning the extrapolation of the present $\langle E \rangle$ results to thermal energies, a linear by-eye extrapolation to thermal would seem to imply a centroid mean energy effectively equal to that of ENDF/B-VIII.0 and JENDL-4.0. However, the total uncertainty, which is almost entirely systematic at the lower incident neutron energies reported here, is well within agreement with the ENDF/B-VIII.0 and JENDL-4.0 thermal

values. The thermal value of JEFF-3.3 may be only be just in agreement with the linearly extrapolated total uncertainty of the present results despite the good agreement with the $\langle E \rangle$ trend shape below $E_n^{\text{inc}} = 10$ MeV.

VII. CONCLUSIONS

An accurate characterization of the energy spectrum of neutrons emitted promptly after neutron-induced fission, i.e., the PFNS, is crucial for understanding the behavior of a variety of nuclear systems. However, the majority of the available PFNS literature data lack the precision and coverage of both incident and outgoing neutron energies required to accurately guide evaluations and fission models [11–13]. With regard to the ^{239}Pu PFNS, multiple data sets were found to contain incorrect assumptions or unknown errors. While corrections could be estimated for some of these errors with a corresponding increased uncertainty, some errors could not be accurately corrected, leading to further increased uncertainties or complete exclusion of data in PFNS evaluations.

The Chi-Nu experiment was designed to measure the PFNS for wide range of incident and outgoing energies with a thorough analysis of systematic uncertainties and extensive analysis documentation. Presented here are the ^{239}Pu PFNS results from the Chi-Nu experiment. These data span outgoing neutron energies from 0.01 to 10.0 MeV and incident neutron energies from 1 to 20 MeV. Two detector arrays were used to cover the entire outgoing neutron energy range of interest. Data from these detectors were correlated with each other and combined to form a single PFNS shape measurement for each incident energy range. Furthermore, these data were correlated across incident neutron energies based on the similar analyses required at each incident neutron energy, yielding a single covariance matrix to describe all of the data reported in this work. This correlation across incident neutron energies made it possible to calculate a covariance matrix of the measured mean PFNS energy trend. The experimental mean energy covariances have never been reported for a PFNS measurement, and these covariances allow for firm statements regarding the *shape* of the mean energy trend to be made for the first time. In addition to statistical uncertainties from the measured data spectrum, background, and MCNP simulations, systematic uncertainties from background normalization, rate dependence of the background shape, PFNS extraction technique, PPAC angular detection efficiencies, fission fragment anisotropies, kinematics, nuclear cross sections used in MCNP, postprocessing parameters for the MCNP simulations, and incident neutron beam wraparound effects were explored for the results shown here. While this list of systematic uncertainty sources is already quite extensive, additional systematics will likely be explored in the future as the analysis of Chi-Nu PFNS data from other isotopes progresses. As such, the authors should be consulted for the latest version of the covariance matrices for Chi-Nu results.

The data shown here provide much-needed guidance on the ^{239}Pu PFNS trends as a function of incident neutron energy, especially with regard to multichance fission and pre-

equilibrium neutron emission processes. The present results agree fairly well with the results of Lestone *et al.*, which have been a strong influence on the low-incident-energy PFNS evaluations. At higher incident energies the present results appear to largely verify the treatment of second-chance fission in ENDF/B-VIII.0 in both PFNS shape and mean PFNS energy. However, third-chance fission does not appear to be present to the extent predicted by ENDF/B-VIII.0 or JEFF-3.3, and JENDL-4.0 appears to agree better with the magnitude of the mean PFNS energies of the present results above 10- to 12-MeV incident neutron energy. The angle-integrated treatment of the pre-equilibrium component of the ^{239}Pu PFNS of the ENDF/B-VIII.0 and JEFF-3.3 evaluations appears to broadly agree with the data shown in this work, though no angle-differentiated information is available from these or any nuclear data evaluation. As such, here we described a procedure for extracting the counts in the well-resolved peak of the pre-equilibrium distribution to estimate the angular distribution of the pre-equilibrium prefission neutron component of the spectrum. The results of this procedure are shown in Ref. [53].

Data from this work are available for inclusion in nuclear data evaluations, and it should be noted that these results supersede those in previous publications of preliminary results. Additionally, while we report here the combined Li-glass-liquid scintillator PFNS across three orders of magnitude of outgoing neutron energy and 20 MeV of incident neutron energies, it is possible to report only a subset of these data, e.g., from a single detector array or over a subset of the reported energies. Although it might at first be assumed that the reported results could be truncated to the desired ranges to obtain the desired data, the covariances of the PFNS may change more than expected. For example, if only the liquid scintillator data were reported, the covariance for the liquid scintillator data alone would be notably different than the liquid scintillator portion of the combined Li-glass-liquid scintillator covariance matrix reported here. Therefore, when these data are used in an evaluation, care should be taken to clearly state how they were used and a proper covariance treatment must be verified to ensure they are used properly.

ACKNOWLEDGMENTS

This work was supported by the U.S. Department of Energy through Los Alamos National Laboratory and Lawrence Livermore National Laboratory. Los Alamos National Laboratory is operated by Triad National Security, LLC, for the National Nuclear Security Administration of the U.S. Department of Energy (Contract No. 89233218CNA000001). Work at Lawrence Livermore National Laboratory was performed under Contract No. DE-AC52-07NA27344. We thank F. David Sattler for design work on the Chi-Nu arrays and Mark Chadwick for guidance and discussions. We also acknowledge the contributions of B. Bucher, B. Perdue, T. Bredeweg, A. Chyzh, E. Kwan, S. Wender, G. Rusev, M. Jandel, S. Sjue, M. E. Rising, C. J. Solomon, I. Stetcu, and J. Lestone to the Chi-Nu project.

- [1] A. E. Walter and A. B. Reynolds, *Fast Breeder Reactors* (Pergamon Press, London, 1981).
- [2] B. E. Watt, *Phys. Rev.* **87**, 1037 (1952).
- [3] J. Terrell, *Phys. Rev.* **113**, 527 (1958).
- [4] G. Vladuca and A. Tudora, *Ann. Nucl. Energy* **28**, 419 (2001).
- [5] P. Talou, R. Vogt, J. Randrup, M. E. Rising, S. A. Pozzi *et al.*, *Eur. Phys. J. A* **54**, 9 (2018).
- [6] R. Vogt, J. Randrup, D. A. Brown, M. A. Descalle, and W. E. Ormand, *Phys. Rev. C* **85**, 024608 (2012).
- [7] V. M. Maslov, Y. V. Porodzinskij, M. Baba, A. Hasegawa, N. V. Kornilov, A. B. Kagalenko, and N. A. Tetereva, *Phys. Rev. C* **69**, 034607 (2004).
- [8] V. M. Maslov, N. V. Kornilov, A. B. Kagalenko, and N. A. Tetereva, *Nucl. Phys. A* **760**, 274 (2005).
- [9] V. M. Maslov, N. A. Tetereva, V. G. Pronyaev, A. B. Kagalenko, K. I. Zolotarev *et al.*, *J. Kor. Phys. Soc.* **59**, 1337 (2011).
- [10] V. A. Rubchenya, *Phys. Rev. C* **75**, 054601 (2007).
- [11] R. Capote, Y.-J. Chen, F.-J. Hamsch, N. V. Kornilov, J. P. Lestone *et al.*, *Nucl. Data Sheets* **131**, 1 (2016).
- [12] D. Neudecker, T. N. Taddeucci, R. C. Haight, H. Y. Lee, M. C. White *et al.*, *Nucl. Data Sheets* **131**, 289 (2016).
- [13] D. Neudecker, P. Talou, T. Kawano, A. Kahler, M. White *et al.*, *Nucl. Data Sheets* **148**, 293 (2018).
- [14] M. B. Chadwick, M. Herman, P. Oblžinský, M. E. Dunn, Y. Danon *et al.*, *Nucl. Data Sheets* **112**, 2887 (2011).
- [15] D. A. Brown, M. B. Chadwick, R. Capote, A. C. Kahler, A. Trkov *et al.*, *Nucl. Data Sheets* **148**, 1 (2018).
- [16] J. P. Lestone and E. F. Shores, *Nucl. Data Sheets* **119**, 213 (2014).
- [17] P. A. Staples, Prompt fission neutron energy spectra induced by fast neutrons, Ph.D. thesis, University of Massachusetts Lowell, 1993.
- [18] J. P. Lestone, Los Alamos National Laboratory Report No. LA-UR-15-23283 (Los Alamos National Laboratory, Los Alamos, NM, 2015).
- [19] P. I. Johansson and B. Holmqvist, *Nucl. Sci. Eng.* **62**, 695 (1977).
- [20] A. Chatillon, G. Bélier, T. Granier, B. Laurent, B. Morillon *et al.*, *Phys. Rev. C* **89**, 014611 (2014).
- [21] T. Granier, *Phys. Proc.* **64**, 183 (2015).
- [22] R. C. Haight, H. Y. Lee, T. N. Taddeucci, J. M. O'Donnell, B. A. Perdue *et al.*, Los Alamos National Laboratory Report No. LA-UR-12-25233 (Los Alamos National Laboratory, Los Alamos, NM, 2012).
- [23] R. C. Haight, H. Y. Lee, T. N. Taddeucci, J. M. O'Donnell, B. A. Perdue *et al.*, Los Alamos National Laboratory Report No. LA-UR-15-27715 (Los Alamos National Laboratory, Los Alamos, NM, 2015).
- [24] R. C. Haight, C. Y. Wu, H. Y. Lee, T. N. Taddeucci, B. A. Perdue *et al.*, *Nucl. Data Sheets* **123**, 130 (2015).
- [25] M. B. Chadwick, P. Oblžinský, M. Herman, N. M. Greene, R. D. McKnight *et al.*, *Nucl. Data Sheets* **107**, 2931 (2006).
- [26] D. Neudecker, R. Capote, D. L. Smith, and T. Burr, *Nucl. Sci. Eng.* **179**, 381 (2015).
- [27] P. Marini, J. Taieb, B. Laurent, G. Belier, A. Chatillon *et al.*, *Phys. Rev. C* **101**, 044614 (2020).
- [28] K. J. Kelly, J. M. O'Donnell, D. Neudecker, M. Devlin, and J. A. Gomez, *Nucl. Instrum. Methods A* **943**, 162449 (2019).
- [29] M. Devlin, J. A. Gomez, K. J. Kelly, R. C. Haight, J. M. O'Donnell *et al.*, *Nucl. Data Sheets* **148**, 322 (2018).
- [30] K. J. Kelly, J. A. Gomez, J. M. O'Donnell, M. Devlin, R. C. Haight *et al.*, in *Proceedings of the 20th Topical Meeting of the Radiation Protection and Shielding Division* (La Grange Park, Illinois, 2018), Los Alamos Report No. LA-UR-18-28140.
- [31] C. Y. Wu, R. A. Henderson, R. C. Haight, H. Y. Lee, T. N. Taddeucci *et al.*, *Nucl. Instrum. Methods A* **794**, 76 (2015).
- [32] G. C. Tyrrell, *Nucl. Instrum. Methods A* **546**, 180 (2005).
- [33] scintacor.com/products/6-lithium-glass.
- [34] www.hamamatsu.com.
- [35] eljentechnology.com/products/liquid-scintillators/ej-301-ej-309.
- [36] www.caen.it/products/sy4527.
- [37] www.caen.it/products/v1730.
- [38] npg.dl.ac.uk/MIDAS.
- [39] J. M. O'Donnell, *Nucl. Instrum. Methods A* **805**, 87 (2016).
- [40] J. K. Dickens, Oak Ridge National Laboratory Report 6462 (Oak Ridge National Laboratory, Oak Ridge, TN, 1988).
- [41] J. K. Dickens, Oak Ridge National Laboratory Report 6463 (Oak Ridge National Laboratory, Oak Ridge, TN, 1988).
- [42] F. J. Saglime, Y. Danon, R. C. Block, M. J. Rapp, R. M. Bahrn *et al.*, *Nucl. Instrum. Methods A* **620**, 401 (2010).
- [43] S. Noda, R. C. Haight, R. O. Nelson, M. Devlin, J. M. O'Donnell *et al.*, *Phys. Rev. C* **83**, 034604 (2011).
- [44] V. N. Kononov, E. D. Poletaev, M. V. Bohovko, L. E. Kazakov, V. M. Timohov *et al.*, *Nucl. Instrum. Methods A* **234**, 361 (1985).
- [45] X-5 Monte Carlo Team, Los Alamos National Laboratory Report No. LA-UR-03-1987 (Los Alamos National Laboratory, Los Alamos, NM, 2003).
- [46] S. A. Pozzi, E. Padovani, and M. Marsequerra, *Nucl. Instrum. Methods A* **513**, 550 (2003).
- [47] S. A. Pozzi, S. D. Clarke, W. J. Walsh, E. C. Miller, J. L. Dolan *et al.*, *Nucl. Instrum. Methods A* **694**, 119 (2012).
- [48] H. Y. Lee, T. N. Taddeucci, R. C. Haight, T. A. Bredeweg, A. Chyzh *et al.*, *Nucl. Instrum. Methods A* **703**, 213 (2013).
- [49] T. N. Taddeucci, R. C. Haight, H. Y. Lee, D. Neudecker, J. M. O'Donnell *et al.*, *Nucl. Data Sheets* **123**, 135 (2015).
- [50] J. Armstrong, F. B. Brown, J. S. Bull, L. Casswell, L. J. Cox *et al.*, Los Alamos National Laboratory Report No. LA-UR-17-29981 (Los Alamos National Laboratory, Los Alamos, NM, 2017).
- [51] C. J. Solomon, C. Bates, and J. Kulesza, Los Alamos National Laboratory Report No. LA-UR-17-21779 (Los Alamos National Laboratory, Los Alamos, NM, 2017).
- [52] K. J. Kelly, J. A. Gomez, J. M. O'Donnell, M. Devlin, R. C. Haight *et al.*, *Nucl. Instrum. Methods A* **954**, 161411 (2020).
- [53] K. J. Kelly, T. Kawano, J. M. O'Donnell, J. A. Gomez, M. Devlin *et al.*, *Phys. Rev. Lett.* **122**, 072503 (2019).
- [54] J. M. O'Donnell, K. J. Kelly, A. E. Lovell *et al.* (unpublished).
- [55] T. N. Taddeucci, Los Alamos National Laboratory Report LA-UR-11-01326 (Los Alamos National Laboratory, Los Alamos, NM, 2011).
- [56] G. Hempel, F. Hopkins, and G. Schatz, *Nucl. Instrum. Methods* **131**, 445 (1975).
- [57] T. N. Taddeucci, Insight regarding dependence of Chi-Nu PFNS results on PPAC efficiency trends (private communication).
- [58] A. S. Vorobyev, A. M. Gagarski, O. A. Shcherbakov, L. A. Vaishene, and A. L. Barabanov, *JETP Lett.* **102**, 203 (2015).
- [59] A. S. Vorobyev, A. M. Gagarski, O. A. Shcherbakov, L. A. Vaishene, and A. L. Barabanov, *JETP Lett.* **107**, 521 (2018).

- [60] L. Blumberg and R. B. Leachman, *Phys. Rev.* **116**, 102 (1959).
- [61] J. E. Simmons and R. L. Henkel, *Phys. Rev.* **120**, 198 (1960).
- [62] R. B. Leachman and L. Blumberg, *Phys. Rev.* **137**, B814 (1965).
- [63] V. G. Nesterov, G. N. Smirenkin, and D. L. Shpak, *Yadern Fiz.* **4**, 993 (1966).
- [64] D. L. Shpak, Y. B. Ostapenko, and G. N. Smirenkin, *Sov. J. Nucl. Phys.* **13**, 547 (1971).
- [65] K. D. Androsenko, G. G. Korolev, and D. L. Shpak, *Vopr. At. Nauki Tekh., Ser. Yad. Konst.* **46**, 9 (1982).
- [66] K. J. Kelly, J. M. O'Donnell, J. A. Gomez, T. N. Taddeucci, M. Devlin *et al.*, *Nucl. Instrum. Methods A* **866**, 182 (2017).
- [67] K. J. Kelly, M. Devlin, J. A. Gomez, J. M. O'Donnell, T. N. Taddeucci *et al.*, *EPJ Web Conf.* **193**, 03003 (2018).
- [68] W. Mannhart, IAEA-TECDOC-410, 158 (International Atomic Energy Agency, Vienna, Austria, 1987).
- [69] D. S. Mather, P. Fieldhouse, and A. Moat, *Nucl. Phys.* **66**, 149 (1965).
- [70] H. Condé, J. Hansén, and M. Holmberg, *J. Nucl. Energy* **22**, 53 (1968).
- [71] M. Soleilhac, J. Frehaut, and J. Gauriau, *J. Nucl. Energy* **23**, 257 (1969).
- [72] R. L. Walsh and J. W. Boldeman, *Ann. Nucl. Sci. Eng.* **1**, 353 (1971).
- [73] F. James and M. Roos, *Comput. Phys. Commun.* **10**, 343 (1975).
- [74] R. Brun and F. Rademakers, *Nucl. Instrum. Methods A* **389**, 81 (1997).
- [75] A. D. Carlson, V. G. Pronyaev, R. Capote, G. M. Hale, Z.-P. Chen *et al.*, *Nucl. Data Sheets* **148**, 143 (2018).
- [76] The Joint Evaluated Fission and Fusion File (JEFF), Version 3.3 www.oecd-nea.org/dbdata/jeff/jeff33/index.html.
- [77] J. P. Lestone and E. F. Shores, Los Alamos National Laboratory Report No. LA-UR-14-24087 (Los Alamos National Laboratory, Los Alamos, NM, 2014).
- [78] T. Kawano, T. Ohsawa, M. Baba, and T. Nakagawa, *Phys. Rev. C* **63**, 034601 (2001).
- [79] H. Feshbach, A. Kerman, and S. Koonin, *Ann. Phys. (NY)* **125**, 429 (1980).
- [80] J. Dobeš and E. Běták, *Z. Phys.* **A310**, 329 (1983).
- [81] E. Gadioli and P. E. Hodgson, *Pre-equilibrium Nuclear Reactions* (Oxford University Press, New York, 1992).
- [82] A. J. Koning and M. C. Duijvestijn, *Nucl. Phys. A* **744**, 15 (2004).
- [83] O. Iwamoto, *J. Nucl. Sci. Technol.* **45**, 910 (2008).
- [84] C. Kalbach and F. M. Mann, *Phys. Rev. C* **23**, 112 (1981).
- [85] K. Shibata, O. Iwamoto, T. Nakagawa, N. Iwamoto, A. Ichihara *et al.*, *J. Nucl. Sci. Technol.* **48**, 1 (2011).